AGU PUBLICATIONS

JGR

Journal of Geophysical Research: Solid Earth

RESEARCH ARTICLE

10.1002/2013JB010614

Key Points:
- Numerical simulations reveal that basins affect the earthquake cycle
- Subbasin events depend both on sediment stiffness and basin depth
- Alternating events may explain shallow slip deficit

Correspondence to:
B. A. Erickson,
berickson@mail.sdsu.edu

Citation:
Erickson, B. A., and E. M. Dunham (2014), An efficient numerical method for earthquake cycles in heterogeneous media: Alternating subbasin and surface-rupturing events on faults crossing a sedimentary basin, *J. Geophys. Res. Solid Earth*, *119*, 3290–3316, doi:10.1002/2013JB010614.

Received 19 AUG 2013
Accepted 3 MAR 2014
Accepted article online 12 MAR 2014
Published online 22 APR 2014

An efficient numerical method for earthquake cycles in heterogeneous media: Alternating subbasin and surface-rupturing events on faults crossing a sedimentary basin

Brittany A. Erickson[1] and Eric M. Dunham[2,3]

[1]Department of Geological Sciences, San Diego State University, San Diego, California, USA, [2]Department of Geophysics, Stanford University, Stanford, California, USA, [3]Institute for Computational and Mathematical Engineering, Stanford University, Stanford, California, USA

Abstract We present an efficient numerical method for earthquake cycle simulations that employs a finite difference discretization of the off-fault material to accommodate spatially variable elastic properties. The method is developed for the two-dimensional antiplane shear problem of a vertical strike-slip fault with rate-and-state friction. We compare earthquake cycles in a homogeneous half-space with those in which the upper portion of the fault cuts through a sedimentary basin. In both cases, we assume velocity-weakening behavior over the full seismogenic depth, even in the basin, to isolate the influence of elastic heterogeneity. In a homogeneous half-space, events rupturing the full seismogenic depth occur periodically. Event sequences are more complex in basin models, with one or several subbasin events confined to the lower section of the fault followed by a much larger, surface-rupturing event that breaks through the basin. This phenomenology emerges only for sufficiently compliant and deep basins. Predicted surface velocities are essentially identical before subbasin events and surface-rupturing events, suggesting that geodetic observations would not be useful in predicting the rupture mode. The alternating sequence of subbasin and surface-rupturing events would complicate interpretation of paleoseismic data. Our results also offer one potential explanation for the shallow slip deficit observed in many recent earthquakes, namely, that these events, which lack appreciable surface slip, are simply one style of rupture. Subsequent events on these faults might be larger, with slip extending all the way to the surface. The 1940 M_w 7.0 and 1979 M_w 6.5 Imperial Valley events might be considered as examples of these two rupture styles.

1. Introduction

Many faults cut through sedimentary basins, and it is desirable to characterize how the compliant materials characteristic of these basins affect earthquake occurrence. The Salton Trough in Southern California, for example, is an ~5 km deep sedimentary basin that surrounds sections of many active faults that are part of the greater southern San Andreas fault system. Recent studies investigating possible disagreements between geologic and geodetic estimates of long-term slip rates on these faults have explored the importance of the heterogeneous material structure [*Fay and Humphreys*, 2005; *Fialko*, 2006; *Lindsey and Fialko*, 2013]. Additionally, while spatial variations in fault frictional properties are well known to control the pattern of coseismic slip and interseismic creep [*Tse and Rice*, 1986; *Lapusta et al.*, 2000; *Lapusta and Rice*, 2003; *Noda and Lapusta*, 2013], the same might also be true for off-fault material properties. Transitions in elastic properties along a fault would introduce heterogeneity in stress from creep or coseismic slip, even for uniform fault slip. These stress heterogeneities would then affect subsequent ruptures. Of course, there are often correlations between frictional properties and lithology. For example, sediments often exhibit velocity-strengthening frictional behavior [*Marone and Scholz*, 1988; *Scholz*, 1998, 2002; *Marone*, 1998; *Verberne et al.*, 2010], particularly at low confining stresses and when shear is distributed. On the other hand, stick-slip has been experimentally observed for sandstones [*Engelder et al.*, 1975] and dolomites [*Weeks and Tullis*, 1985]. Recent work by *Kohli and Zoback* [2013] on a wide range of shales shows both velocity-weakening and velocity-strengthening behaviors, with the latter arising only for sufficiently high clay content.

There are many documented examples of coseismic slip in large earthquakes failing to penetrate through sedimentary layers to reach Earth's surface, leading to what is known as the shallow slip deficit [*Fialko et al.*,

2005]. Several examples, as discussed by *Kaneko and Fialko* [2011], include the 1992 Landers, 1999 Hector Mine, 2003 Bam, 2010 Haiti, and 2010 Sierra El Mayor-Cucupah earthquakes, and there are many others. In some cases, the upper portion of the fault slips aseismically [*Bilham*, 1989; *Wei et al.*, 2013], consistent with velocity-strengthening response of sediments. However, other faults do not exhibit shallow aseismic creep, or at least not enough to balance the long-term motion, and some alternative explanation must be sought for how deformation is ultimately accommodated near the surface. One possibility is distributed inelastic strains within the shallow crust, but recent modeling efforts by *Kaneko and Fialko* [2011] have suggested that inelastic off-fault strains are unlikely to be large enough to explain the observed shallow slip deficit.

In the latter part of this work, we offer another possible explanation based on earthquake cycle simulations in a heterogeneous elastic medium. We suggest that there may exist distinct modes of rupture, with some events nucleated at depth arresting upon entering sediments, and others continuing to the surface in much larger events that relieve the shallow slip deficit. The 1979 M_w 6.5 Imperial Valley event provides an example of the former, with slip largely confined beneath a 4 km thick sedimentary cover [*Hartzell and Heaton*, 1983; *Archuleta*, 1984]. In contrast, the 1940 M_w 7.0 Imperial Valley earthquake, which ruptured, in part, the same section of the Imperial Fault as the 1979 event, featured several meters of surface slip over much of its extent [*Sharp et al.*, 1982; *Sieh*, 1996; *Rockwell and Klinger*, 2013].

Regardless of the particular fault behavior, it is clearly essential to develop numerical methods for earthquake cycles that rigorously account for all of these different types of heterogeneities. Modeling the full cycle, however, presents great computational challenges due to the wide range of relevant scales in both space and time. It is currently necessary to artificially enhance frictional properties (specifically, the state evolution distance) to render nucleation lengths numerically resolvable on large-scale faults [*Rice*, 1993]. Even with this approximation, there remains the need to resolve both slow loading during the interseismic period of hundreds of years, during which the deep portions of faults creep at several to tens of millimeters per year, and rapid coseismic sliding, lasting tens of seconds, at several meters per second. Adaptive time-stepping algorithms are therefore necessary. It is also possible to gain efficiency by neglecting inertial effects during the interseismic period and solving the equilibrium equations in place of the full momentum balance.

Lapusta et al. [2000] highlight some of the methods for handling varying time scales in earthquake cycle simulations. These include the methods of *Okubo* [1989] and *Shibazaki and Matsu'ura* [1996], which involve switching from static elasticity into the dynamic regime once an event nucleates. *Lapusta et al.* [2000] present a boundary integral equation method that handles cycle models within a unified computational framework that avoids abrupt transitions between static and dynamic elasticities. Related efforts, like those presented in *Tullis et al.* [2012, and references therein] (such as the earthquake simulators of *Rundle* [1988], *Ward* [1996], *Pollitz* [2012], and *Dieterich and Richards-Dinger* [2010]), have focused on approximate methods for modeling seismicity patterns on complex fault networks. All of these methods are based on the boundary element method. Like the boundary integral equation method, current boundary element codes are restricted to faults in uniform, linear elastic whole- and half-spaces. A notable exception in this line of work is the spectral element method of *Kaneko et al.* [2011], which is capable of incorporating variable material properties.

In this work, we present an efficient finite-difference method for earthquake cycles in an elastic medium having arbitrary variations in material properties. The method is developed specifically for the classic two-dimensional antiplane shear problem of a vertical strike-slip fault in a linear elastic half-space. The fault is governed by a rate-and-state friction law with depth-dependent parameters. Our particular interest is the influence of a compliant sedimentary basin on earthquake sequences. Our intent in this initial study is to isolate the influence of elastic heterogeneity, so we neglect possible correlations between lithology and frictional properties (which might suggest using velocity-strengthening properties within the basin). The system is loaded at the remote boundaries to capture the effect of slow tectonic forcing. To facilitate efficient solution, we employ the radiation-damping approximation [*Rice*, 1993], rather than rigorously including inertial dynamics.

The equations of linear elasticity are discretized using second-order accurate summation by parts (SBP) finite differences for variable coefficient problems [*Mattsson and Nordström*, 2004; *Mattsson et al.*, 2008, 2009; *Mattsson*, 2011], with weak enforcement of boundary conditions through the simultaneous-approximation-term (SAT) technique. Finite difference operators satisfying an SBP rule are obtained by

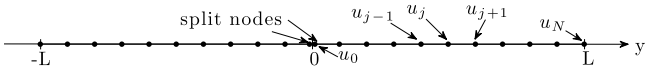

Figure 1. One-dimensional problem domain. Fault lies at interface $y = 0$ with split nodes on either side. Symmetries of the problem allow us to restrict attention to one side of the domain, $y \in [0, L]$, which is discretized with a uniform grid spacing $h = L/N$ at $N + 1$ points.

applying central difference operators in the interior of the computational domain, with a transition to one-sided approximations toward the boundary. Rather than strong enforcement of boundary conditions (also known as injection), where the grid data are overwritten with the boundary data, the SAT method weakly enforces boundary conditions through penalty terms added to the spatially discretized system of equations. The combined SBP-SAT approach permits us to prove both accuracy and stability of the overall method. The SBP-SAT spatial discretization is obtained by analyzing the full elastodynamic problem prior to neglecting the inertial term, a technique frequently done when solving steady state problems in computational fluid dynamics [*Nordström et al.*, 2007; *Eriksson and Nordström*, 2009; *Hicken and Zingg*, 2011]. Provided that the underlying mathematical problem is well posed, in the sense that a unique solution exists depending continuously on the data of the problem (initial/boundary conditions and any source terms), accuracy and stability guarantee that our numerical solution converges toward the true solution under mesh refinement [*Gustafsson et al.*, 1995].

The paper is organized as follows: The numerical method is developed in sections 2–7, and verification tests are presented in section 8. In section 9 we apply the method to study earthquake cycles in sedimentary basins, with concluding discussion of the overall project in section 10. Readers interested in only the basin cycle simulations can proceed directly to section 9. The method development and verification in sections 2–8 is broken down in the following manner. We start with a 1-D version of our 2-D model in order to introduce the governing equations and boundary conditions (section 2) and numerical method (section 3) in a simplified setting. The 2-D problem is presented in section 4, and its numerical discretization is given in section 5. Section 6 presents the fault friction law. Section 7 describes our adaptive time-stepping method. We then develop an analytical solution to the governing equations and use that as the basis for convergence tests in section 8.

2. Governing Equations (1-D)

In this section we consider a 1-D analog of our full 2-D model which will introduce the governing equations, geometry, and boundary conditions. It also provides a simplified setting in which to show how the semidiscrete problem captures several features of its continuous counterpart. The elastic wave equation with spatially variable material properties is

$$\rho \frac{\partial^2 u}{\partial t^2} = \frac{\partial}{\partial y}\left(\mu \frac{\partial u}{\partial y}\right), \quad y \in [-L, L], \quad t \geq 0, \tag{1}$$

where $u(y, t)$ is the displacement and the shear wave speed $c_s = \sqrt{\mu/\rho}$ depends on the material density $\rho = \rho(y)$ and shear modulus $\mu = \mu(y)$. Denoting the time derivative of a field u by $\dot{u}$ (although in some cases we will use d/dt for notational ease), the initial conditions in displacement and velocity are given by

$$u(y, 0) = u_0(y), \quad y \in [-L, L] \tag{2}$$

$$\dot{u}(y, 0) = v_0(y), \quad y \in [-L, L], \tag{3}$$

respectively.

Suppose that $y = 0$ is an interface at the center of the domain $[-L, L]$ (Figure 1) and that the system is loaded at the remote boundaries $y = -L, y = L$ by displacement (Dirichlet) boundary conditions: $u(-L, t) = g_r^{-L}(t)$ and $u(L, t) = g_r^{L}(t)$. We assume that the material properties ρ and μ are symmetric about the interface $y = 0$ and that $-g_r^{-L}(t) = g_r^{L}(t)$ (which we denote by $g_r(t)$). Furthermore, there are two interface conditions that must be satisfied. The first is a jump condition in displacement $u(0^+, t) - u(0^-, t) = \Delta u(t)$ (where Δu can be thought of as slip across a fault interface) and the second is that the traction components of stress be continuous across the interface. Denoting stress by $\sigma(y, t) = \mu(y)\frac{\partial u}{\partial y}(y, t)$ the second interface condition means

that $\sigma(0^+, t) = \sigma(0^-, t)$. With these assumptions and interface conditions, the field $u(y, t)$ is antisymmetric about the interface $y = 0$; thus, for computational purposes, we can then restrict attention to the right half of the domain. One may then impose a boundary condition at $y = 0$, either on traction $\sigma(0, t)$ or on displacement ($u(0, t) = \Delta u/2$) with the understanding that the field $u(y, t)$ in the left half of the domain is the antisymmetric equivalent such that both interface conditions are satisfied. We will assume the left boundary condition at $y = 0$ is a traction (Neumann) boundary condition defined by data $g_l(t)$, in order to show how different types of boundary conditions are treated. Thus, we consider the following boundary conditions:

$$\sigma(0, t) = g_l(t) \tag{4}$$

$$u(L, t) = g_r(t). \tag{5}$$

In formulating an initial boundary value problem like (1)–(5), we would like to ensure that it has a unique solution and that in the case of homogeneous boundary conditions and no body forces, the total energy of the system is conserved. These requirements are central to the concept of well posedness. Assuming a unique solution to (1)–(5) exists, energy conservation can be shown through the so-called energy method [*Gustafsson et al.*, 1995]. An energy estimate can be understood as showing the balance of total mechanical energy in the elastic body by work done (or energy dissipated) at the system's boundaries (or energy conservation, in the absence of nonzero boundary data or source terms). Multiplying equation (1) by $\dot{u}$ and integrating by parts reveals the energy balance:

$$\frac{\mathrm{d}}{\mathrm{d}t}\left(\frac{1}{2}||\sqrt{\rho}\dot{u}||^2 + \frac{1}{2}||\sqrt{\mu}\frac{\partial u}{\partial y}||^2\right) = \sigma\dot{u}|_0^L = \sigma(L)\dot{g}_r - g_l(t)\dot{u}(0) \tag{6}$$

$$= 0 \tag{7}$$

where the left-hand side of equation (6) defines the total mechanical energy $E = \frac{1}{2}||\sqrt{\rho}\dot{u}||^2 + \frac{1}{2}||\sqrt{\mu}\frac{\partial u}{\partial y}||^2$ as the sum of the kinetic and strain energy, and $||v||^2 = (v, v) = \int_0^L v^2 \mathrm{d}y$ describes a norm on the space of square-integrable functions L^2. Equation (6) demonstrates that the rate of change in E is determined by the work rate per unit surface area (the product of shear stress and particle velocity) at the system's boundaries. Energy conservation, as given by equation (7), results from our assumption of homogeneous boundary data ($g_l = g_r = 0$). This assumption is made for the energy method analysis only, as the results extend to general, inhomogeneous boundary data (see Appendix A for more details).

3. Semidiscrete Equations (1-D)

Spatially variable material properties often make analytical solutions to equations (1)–(5) difficult to obtain, and one looks for numerical solutions. A semidiscretization (i.e., spatial discretization) of (1)–(5) for $y \in [-L, L]$ is done with split nodes at the interface $y = 0$. Symmetries of the problem (described in section 2) allow us to consider one side of the domain, discretizing at $N + 1$ uniformly spaced grid points (including the boundary points, see Figure 1) with grid spacing $h = L/N$. We use the second-order-accurate, narrow stencil second-derivative SBP operators for problems with variable coefficients [*Mattsson and Nordström*, 2004; *Mattsson*, 2011] and weak enforcement of boundary conditions to obtain the semidiscretization:

$$\rho\mathbf{u}_{tt} = \mathbf{D}_2^{\mu}\mathbf{u} + \mathbf{p}_l + \mathbf{p}_r \tag{8}$$

where

$$\mathbf{p}_l = \alpha_0\mathbf{H}^{-1}\mathbf{e}_0\left[(\boldsymbol{\mu}\mathbf{B}\mathbf{S}\mathbf{u})_0 - g_l\right] \tag{9}$$

$$\mathbf{p}_r = \alpha_1\mu_N\mathbf{H}^{-1}\mathbf{e}_N\left[u_N - g_r\right] + \beta\mathbf{H}^{-1}(\boldsymbol{\mu}\mathbf{B}\mathbf{S})^T\mathbf{e}_N\left[u_N - g_r\right] \tag{10}$$

and $\mathbf{u}$ now refers to the vector of grid data (or grid function)

$$\mathbf{u} = \mathbf{u}(t) = [u_0(t), u_1(t), \ldots, u_N(t)]^T. \tag{11}$$

The subscript notation $u_j = u_j(t) \approx u(y_j, t)$ for $j = 0, 1, \ldots N$ defines the numerical approximation to the solution at grid point $y_j = jh$. Initial condition (2) is imposed by setting

$$\mathbf{u}(0) = u_0(y_j), \quad j = 0, 1, \ldots N, \tag{12}$$

and initial condition (3) can be imposed in the time integration method in a stable way [e.g., *Strikwerda*, 2004, p. 197]. All matrix operators defined in this section are square matrices of size $(N+1)\times(N+1)$. Diagonal matrices are denoted by $\boldsymbol{\rho}$ and $\boldsymbol{\mu}$ and given by $\boldsymbol{\rho} = \text{diag}(\rho_0, \rho_1, \ldots, \rho_{N-1}, \rho_N)$, $\boldsymbol{\mu} = \text{diag}(\mu_0, \mu_1, \ldots, \mu_{N-1}, \mu_N)$, where $\rho_j = \rho(y_j)$ and $\mu_j = \mu(y_j)$.

The first term on the right of equation (8) defines the differentiation matrix arising from a second-order accurate, narrow stencil, difference approximation:

$$\mathbf{D}_2^{\mu} = \mathbf{H}^{-1}(-\mathbf{M}^{\mu} + \boldsymbol{\mu}\mathbf{B}\mathbf{S}) \approx \frac{\partial}{\partial y}\left[\mu \frac{\partial}{\partial y}\right], \tag{13}$$

which, in the interior of the domain, contains the standard centered difference approximation to second spatial derivatives with variable coefficients [*Zikanov*, 2011]

$$\frac{\partial}{\partial y}\left[\mu \frac{\partial u}{\partial y}\right]_i \approx \frac{\left(\frac{1}{2}\mu_{i-1} + \frac{1}{2}\mu_i\right)u_{i-1} - \left(\frac{1}{2}\mu_{i-1} + \mu_i + \frac{1}{2}\mu_{i+1}\right)u_i + \left(\frac{1}{2}\mu_i + \frac{1}{2}\mu_{i+1}\right)u_{i+1}}{h^2}. \tag{14}$$

In addition, $\mathbf{H} = h\,\text{diag}\left(\frac{1}{2}, 1, 1, \ldots, 1, 1, \frac{1}{2}\right)$ is a diagonal matrix defining a discrete inner product

$$(\mathbf{u}, \mathbf{v})_H = \mathbf{u}^T\mathbf{H}\mathbf{v}, \tag{15}$$

and the associated discrete H norm (a discrete approximation to the L^2 norm)

$$||\mathbf{u}||_H^2 = \mathbf{u}^T\mathbf{H}\mathbf{u}. \tag{16}$$

Matrix $\mathbf{B} = \text{diag}(-1, 0, \ldots, 0, 1)$, and $\mathbf{S}$ is $1/h$ times the identity matrix, but with the first and last rows modified to include a second-order accurate finite difference approximation to the first spatial derivative on the boundary:

$$\mathbf{S} = \frac{1}{h}\begin{bmatrix} -\frac{3}{2} & 2 & -\frac{1}{2} & & \\ & 1 & & & \\ & & \ddots & & \\ & & & 1 & \\ & & \frac{1}{2} & -2 & \frac{3}{2} \end{bmatrix}.$$

The interior stencil of $\mathbf{M}^{\mu}$ at row i is

$$m_{i,i-1} = -\frac{1}{2}\mu_{i-1} - \frac{1}{2}\mu_i \tag{17}$$

$$m_{i,i} = \frac{1}{2}\mu_{i-1} + \mu_i + \frac{1}{2}\mu_{i+1} \tag{18}$$

$$m_{i,i+1} = -\frac{1}{2}\mu_i - \frac{1}{2}\mu_{i+1} \tag{19}$$

for $i = 3, \ldots N-3$. The left and right boundary closures of $\mathbf{M}^{\mu}$ are derived so that $\mathbf{D}_2^{\mu}$ transitions to one-sided differences at the boundaries in a particular way that ensures provable stability. These details can be found in *Mattsson* [2011]. Note that since the grid vector $\mathbf{u}$ includes the boundary nodes u_0 and u_N, $\mathbf{H}^{-1}(-\mathbf{M}^{\mu} + \mathbf{BS})\mathbf{u}$ approximates second spatial derivatives at the boundaries as well.

The SAT penalty vectors $\mathbf{p}_l$ and $\mathbf{p}_r$ on the right of equation (8) (and defined by (9) and (10)) impose the two boundary conditions (4)–(5) weakly. $(\mathbf{BSu})_0$ computes a finite difference approximation to the first derivative of the solution at the boundary $y = 0$; thus, $(\boldsymbol{\mu}\mathbf{BSu})_0$ approximates the stress at $y = 0$. The vectors

$$\mathbf{e}_0 = [1, 0, \ldots, 0, 0]^T, \quad \mathbf{e}_N = [0, 0, \ldots, 0, 1]^T$$

are standard basis vectors in $\mathbb{R}^{N+1}$, and α_0, α_1, and β are scalars known as penalty parameters. The term multiplying α_0 enforces the stress boundary condition weakly. The two terms multiplying α_1 and β are required for the weak enforcement of the displacement boundary condition [*Mattsson et al.*, 2009]. The term multiplying α_1 penalizes the grid point on the boundary, whereas the term multiplying β enforces the displacement boundary condition weakly at all the grid points making up the boundary derivative.

Given a finite difference approximation to first spatial derivatives $\mathbf{D} \approx \partial/\partial y$, it is possible to apply this operator twice to obtain an approximation to the second spatial derivative. However, it was shown in *Mattsson and Nordström* [2004] that this procedure increases the internal width of the scheme and the internal error and cannot capture the π mode (highest wave number mode that exists on the grid) that is often associated with spurious oscillations in the numerical solution. The operator $\mathbf{M}^{\mu}$ is a narrow stencil operator which is related to the first derivative operator $\mathbf{D}$ through the following relation:

$$\mathbf{M}^{\mu} = \mathbf{D}^T \mathbf{H} \boldsymbol{\mu} \mathbf{D} + \mathbf{R}^{\mu} \tag{20}$$

where

$$\mathbf{R}^{\mu} = \frac{h^7}{4} \mathbf{D}_2^T \mathbf{C}_2 \boldsymbol{\mu} \mathbf{D}_2 \tag{21}$$

is a positive semidefinite remainder term which introduces a small numerical energy dissipation term into the semidiscrete energy estimate. This term, which vanishes with mesh refinement, is a useful mechanism for damping spurious oscillations [*Mattsson*, 2011]. The remaining operators defined in this section are given in Appendix B. With equation (20) in mind, we define a second discrete norm we refer to as the discrete energy norm:

$$||\mathbf{u}||_E^2 = \frac{1}{2} \mathbf{u}_t^T \mathbf{H} \boldsymbol{\rho} \mathbf{u}_t + \frac{1}{2} \mathbf{u}^T \mathbf{M}^{\mu} \mathbf{u} \tag{22}$$

where the discrete total mechanical energy $\mathbf{E} \equiv ||\mathbf{u}||_E^2$ is the sum of the discrete kinetic and strain energy.

Given a discretization to a well-posed problem, we need to ensure that the numerical solution converges to the solution of the continuous problem under mesh refinement. This is guaranteed if the discretization is consistent (order of accuracy greater than zero) and stable [*Gustafsson et al.*, 1995]. By construction, discretization (8) is second-order accurate and therefore consistent. Establishing stability of a discretization can be thought of as the discrete analog to well posedness and guarantees that solutions remain bounded as $h \to 0$. One method for proving stability is by obtaining a semidiscrete analog to the energy balance (6). By multiplying (8) by $\mathbf{u}_t^T \mathbf{H}$ and adding the transpose, we obtain the rate of change of the discrete energy

$$\begin{aligned} \frac{\mathrm{d}}{\mathrm{d}t} \left(\frac{1}{2} \mathbf{u}_t^T \mathbf{H} \boldsymbol{\rho} \mathbf{u}_t + \frac{1}{2} \mathbf{u}^T \mathbf{M}^{\mu} \mathbf{u} \right) = (\mathbf{u}_t)_0 \mu_0 (\mathbf{BSu})_0 + (\mathbf{u}_t)_N \mu_N (\mathbf{BSu})_N + \\ + BT_l + BT_r \end{aligned} \tag{23}$$

where

$$BT_l = \alpha_0 (\mathbf{u}_t)_0 \left[\mu_0 (\mathbf{BSu})_0 - g_l \right] \tag{24}$$

$$BT_r = \mu_N \alpha_1 (\mathbf{u}_t)_N \left[u_N - g_r \right] + \beta (\boldsymbol{\mu} \mathbf{BSu}_t)_N \left[u_N - g_r \right]. \tag{25}$$

Equation (23) is the discrete analog of the continuous energy balance (6). The left-hand side of (23) represents the rate of change of the discrete total mechanical energy $\mathbf{E}$ as defined by the discrete energy norm in equation (22). The terms inside the time derivative on the left-hand side are the discrete analogs of the kinetic and strain energy. The first two terms on the right of equation (23) mimic corresponding terms on the right-hand side of equation (6) after integrating by parts (hence the name summation by parts). The boundary terms BT refer to the contributions from the SAT vectors $\mathbf{p}_l, \mathbf{p}_r$ enforcing the boundary conditions weakly. A semidiscretization is said to be strictly stable if the semidiscrete problem dissipates energy at least as fast as its continuous counterpart [*Gustafsson et al.*, 1995; *Nordström*, 2006]. We show in Appendix B that the right-hand side of (23) is ≤ 0 (meaning energy is either conserved or dissipated) if the penalty parameters satisfy $\alpha_0 = -1$, $\beta = 1$, and $\alpha_1 \leq -13/h$. These conditions show that (8) defines a second-order accurate, strictly stable discretization to the initial boundary value problem (1)–(5). Thus, numerical solutions will converge to the solution of the continuous problem under mesh refinement.

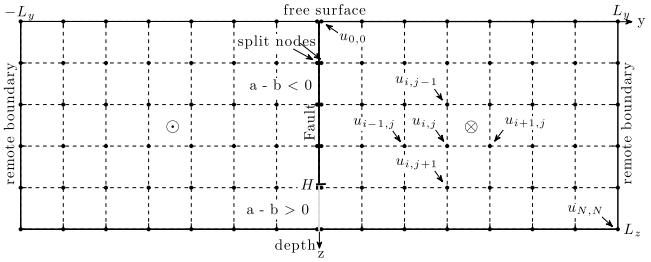

Figure 2. Schematic diagram of our 2-D model, showing cross section of a vertical strike-slip fault embedded in a heterogeneous half-space, subject to antiplane shear deformation. The 1-D fault at $y = 0$ is governed by rate-and-state friction with depth-variable parameters. The elasticity equations are discretized using finite differences. Traction-free boundary conditions are applied at Earth's surface and at depth, and the system is loaded remotely with a displacement boundary condition corresponding to far-field plate motion.

4. Governing Equations (2-D)

The analysis in sections 2 and 3 provides us with the tools to derive the discretization for the problem in 2-D, which will serve as the framework for our simulations. We consider antiplane shear deformation where the only nonzero component of displacement is in the x direction (in and out of the plane, see Figure 2). Substituting Hooke's law into momentum balance yields the elastic wave equation in 2-D:

$$\rho\frac{\partial^2 u}{\partial t^2} = \frac{\partial}{\partial y}\left(\mu\frac{\partial u}{\partial y}\right) + \frac{\partial}{\partial z}\left(\mu\frac{\partial u}{\partial z}\right), \quad (y,z) \in [-L_y, L_y] \times [0, L_z]. \tag{26}$$

As described for the 1-D problem in section 2, symmetries of the material properties, boundary conditions, and interface conditions across the fault $y = 0$ allow us to consider only one side of the domain, $\Omega = [0, L_y] \times [0, L_z]$. We enforce a displacement (Dirichlet) boundary condition on the fault, and we show in section 7 how to determine that displacement in a manner that is consistent with the rate-and-state friction law. Earth's free surface at $z = 0$ is governed by a traction-free (Neumann) boundary condition. Because our method involves a volume discretization, we must also specify artificial boundary conditions at the remaining two boundaries (the remote lateral boundary and the boundary at depth). We choose to load the system at the remote boundary $y = L_y$ by imposing a displacement boundary condition given by the far-field plate rate of $V_p \approx 35$ mm/a. We take the boundary at depth to be traction-free, as is frequently done in similar problems [*Fay and Humphreys*, 2005]. This approximation has minimal influence on the solution, provided that the computational domain is truncated at some depth far greater than the seismogenic depth H. This is because at those depths, if creep along the planar fault approaches a constant rate independent of depth, then displacement also becomes independent of depth such that $\partial u/\partial z$ and the associated shear stress component exerting tractions on the lower boundary are approximately zero.

We can write the boundary data generically as g_f, g_r, g_s, and g_d for the fault, remote, surface, and depth boundaries, respectively (see Figure 2),

$$u(0,z,t) = g_f(z,t) \tag{27}$$

$$u(L_y,z,t) = g_r(z,t) \tag{28}$$

$$\mu(y,0)\frac{\partial u}{\partial z}\bigg|_{z=0} = g_s(y,t) \tag{29}$$

$$\mu(y,L_z)\frac{\partial u}{\partial z}\bigg|_{z=L_z} = g_d(y,t), \tag{30}$$

although keeping in mind that for our simulations, the free surface conditions imply that $g_s(y,t) = g_d(y,t) = 0$, and at the remote boundary $g_r(z,t) = V_p t/2$.

As done for the 1-D problem in section 2, we now show the continuous problem (26)–(30) plus appropriate initial conditions leads to a well-posed mathematical problem. This can be done by establishing

energy conservation in the absence of nonzero boundary data or source terms, recognizing that the results extend to general, nonzero boundary data (see also Appendix A for more details). Multiplying (26) by u_t and integrating over the domain yields

$$\frac{d}{dt}\left[\frac{1}{2}||\sqrt{\rho}u_t||^2 + \frac{1}{2}\left(||\sqrt{\mu}u_y||^2 + ||\sqrt{\mu}u_z||^2\right)\right] = B_r + B_f + B_s + B_d \tag{31}$$

where the left-hand side of (31) corresponds to the rate of change of total mechanical energy E and

$$B_r = \int_0^{L_z} \mu u_y u_t \mathrm{d}z \tag{32}$$

$$B_f = -\int_0^{L_z} \mu u_y u_t \mathrm{d}z \tag{33}$$

$$B_s = -\int_0^{L_y} \mu u_z u_t \mathrm{d}y \tag{34}$$

$$B_d = \int_0^{L_y} \mu u_z u_t \mathrm{d}y \tag{35}$$

correspond to the rate at which work is done on the elastic body by boundary tractions. For homogeneous boundary conditions, $g_r = g_f = g_s = g_d = 0$, the boundary terms B_r, B_f, B_s, and B_d vanish and energy is conserved.

5. Semidiscrete Equations (2-D)

For the 2-D discretization of (26)–(30), we will often utilize the Kronecker product:

$$\mathbf{A} \otimes \mathbf{B} := \begin{bmatrix} a_{0,0}B & \cdots & a_{0,N}B \\ \vdots & & \vdots \\ a_{N,0}B & \cdots & a_{N,N}B \end{bmatrix}.$$

We discretize the domain $[0, L_y] \times [0, L_z]$ with an $(N_y + 1) \times (N_z + 1)$-point grid, defined by

$$y_i = ih_y, \quad i = 0, 1, ..., N_y, h_y = L_y/N_y \tag{36}$$

$$z_i = ih_z, \quad i = 0, 1, ..., N_z, h_z = L_z/N_z \tag{37}$$

where h_z and h_y are the grid spacings in each direction. Thus,

$$u_{i,j} \approx u(y_i, z_j)$$

is the discrete approximation to the solution at grid point (y_i, z_j). We now define the grid vector $\mathbf{u}$ as a vector of vectors. We first define the discrete solution vector

$$\mathbf{u}_i = [u_{i,0}, u_{i,1}, \ldots, u_{i,N_z-1}, u_{i,N_z}]^T \quad \text{for } i = 0, \ \ldots, \ N_y$$

so that

$$\mathbf{u} = [\mathbf{u}_0^T, \mathbf{u}_1^T, \ldots, \mathbf{u}_{N_y}^T]^T.$$

To distinguish whether a 2-D operator $\mathbf{P}$ is operating in the y or z direction, we use the notations $\mathbf{P}_y$ and $\mathbf{P}_z$, respectively. A semidiscretization of (26) using the SBP-SAT technique described in section 3 is

$$\boldsymbol{\rho}\mathbf{u}_{tt} = \mathbf{D}_{2y}^{\mu}\mathbf{u} + \mathbf{D}_{2z}^{\mu}\mathbf{u} + \mathbf{p}_f + \mathbf{p}_r + \mathbf{p}_s + \mathbf{p}_d \tag{38}$$

where

$$\mathbf{D}_{2y}^{\mu} = (\mathbf{H}_y^{-1} \otimes \mathbf{I}_z)\left[-(\mathbf{D}_y \otimes \mathbf{I}_z)^T \boldsymbol{\mu}(\mathbf{H}_y \otimes \mathbf{I}_z)(\mathbf{D}_y \otimes \mathbf{I}_z) - \mathbf{R}_y^{\mu} + \boldsymbol{\mu}(\mathbf{B}_y\mathbf{S}_y \otimes \mathbf{I}_z)\right] \tag{39}$$

$$\mathbf{D}_{2z}^{\mu} = (\mathbf{I}_y \otimes \mathbf{H}_z^{-1}) \left[-(\mathbf{I}_y \otimes \mathbf{D}_z)^T \boldsymbol{\mu} (\mathbf{I}_y \otimes \mathbf{H}_z)(\mathbf{I}_y \otimes \mathbf{D}_z) - \mathbf{R}_z^{\mu} + \boldsymbol{\mu}(\mathbf{I}_y \otimes \mathbf{B}_z \mathbf{S}_z) \right] \tag{40}$$

$$\mathbf{R}_y^{\mu} = \frac{h_y^7}{4} \left(\mathbf{D}_{2y}^T \otimes \mathbf{I}_z \right) \left(\mathbf{C} \otimes \mathbf{I}_z \right) \mu \left(\mathbf{D}_{2y} \otimes \mathbf{I}_z \right) \tag{41}$$

$$\mathbf{R}_z^{\mu} = \frac{h_z^7}{4} \left(\mathbf{I}_y \otimes \mathbf{D}_{2z}^T \right) \left(\mathbf{I}_y \otimes \mathbf{C} \right) \mu \left(\mathbf{I}_y \otimes \mathbf{D}_{2z} \right) \tag{42}$$

where all matrix operators are of size $(N_y + 1)(N_z + 1) \times (N_y + 1)(N_z + 1)$. $\mathbf{I}$ is the identity matrix, and matrices $\mathbf{H}$, $\mathbf{D}$, $\mathbf{B}$, $\mathbf{S}$, $\mathbf{R}$, and $\mathbf{C}$ are given in section 3 and Appendix B. Matrices $\mathbf{D}_{2y}$ and $\mathbf{D}_{2z}$ approximate $\partial^2/\partial y^2$ and $\partial^2/\partial z^2$, respectively. Boundary conditions are enforced weakly in (38) through the SAT vectors:

$$\mathbf{p}_f = \alpha_f \boldsymbol{\mu} (\mathbf{H}_y^{-1} \otimes \mathbf{I}_z) \tilde{\mathbf{E}}_f \left(\mathbf{u}_f - \mathbf{g}_f \right) + \beta (\mathbf{H}_y^{-1} \otimes \mathbf{I}_z) [\boldsymbol{\mu} (\mathbf{B}_y \mathbf{S}_y \otimes \mathbf{I}_z)]^T \tilde{\mathbf{E}}_f \left(\mathbf{u}_f - \mathbf{g}_f \right) \tag{43}$$

$$\mathbf{p}_r = \alpha_r \boldsymbol{\mu} (\mathbf{H}_y^{-1} \otimes \mathbf{I}_z) \tilde{\mathbf{E}}_r \left(\mathbf{u}_r - \mathbf{g}_r \right) + \beta (\mathbf{H}_y^{-1} \otimes \mathbf{I}_z) [\boldsymbol{\mu} (\mathbf{B}_y \mathbf{S}_y \otimes \mathbf{I}_z)]^T \tilde{\mathbf{E}}_r \left(\mathbf{u}_r - \mathbf{g}_r \right) \tag{44}$$

$$\mathbf{p}_s = \alpha_s (\mathbf{I}_y \otimes \mathbf{H}_z^{-1}) \tilde{\mathbf{E}}_s \left([\boldsymbol{\mu} (\mathbf{I}_y \otimes \mathbf{B}_z \mathbf{S}_z) \mathbf{u}]_s + \mathbf{g}_s \right) \tag{45}$$

$$\mathbf{p}_d = \alpha_d (\mathbf{I}_y \otimes \mathbf{H}_z^{-1}) \tilde{\mathbf{E}}_d \left([\boldsymbol{\mu} (\mathbf{I}_y \otimes \mathbf{B}_z \mathbf{S}_z) \mathbf{u}]_d - \mathbf{g}_d \right) \tag{46}$$

where $\alpha_f, \alpha_r, \alpha_s, \alpha_d$, and β are the penalty parameters. The operators

$$\tilde{\mathbf{E}}_f = \mathbf{e}_0^y \otimes \mathbf{I}_z, \quad \tilde{\mathbf{E}}_r = \mathbf{e}_N^y \otimes \mathbf{I}_z, \tag{47}$$

$$\tilde{\mathbf{E}}_s = \mathbf{I}_y \otimes \mathbf{e}_0^z, \quad \tilde{\mathbf{E}}_d = \mathbf{I}_y \otimes \mathbf{e}_N^z \tag{48}$$

map the boundary grid points to full length vectors. Defined in section 3 are the 1-D vectors, $\mathbf{e}_0^z, \mathbf{e}_N^z, \mathbf{e}_0^y$, and $\mathbf{e}_N^y$, of size $N_z + 1$ and $N_y + 1$, denoted by the superscript. In the 2-D case here, $\boldsymbol{\mu}$ is a diagonal matrix formed by

$$\boldsymbol{\mu}_i = [\mu_{i,0} \ \mu_{i,1} \ \ldots \ \mu_{i,N_z-1} \ \mu_{i,N_z}]^T \quad \text{for } i = 0, \ \ldots, \ N_y$$

where

$$\mu_{i,j} = \mu(y_i, z_j)$$

thus

$$\boldsymbol{\mu} = \text{diag}(\boldsymbol{\mu}_0^T, \boldsymbol{\mu}_1^T, \ldots, \boldsymbol{\mu}_{N_y-1}^T, \boldsymbol{\mu}_{N_y}^T).$$

The matrix $\boldsymbol{\rho}$ is formed similarly. Matrices $\mathbf{H}_y$ and $\mathbf{H}_z$ together form the discrete H norm (approximating the L^2 norm) in 2-D:

$$||\mathbf{u}||_H^2 = \mathbf{u}^T (\mathbf{H}_y \otimes \mathbf{H}_z) \mathbf{u} \tag{49}$$

and the discrete energy norm in 2-D

$$||\mathbf{u}||_E^2 = \frac{1}{2} \mathbf{u}_t^T (\mathbf{H}_y \otimes \mathbf{H}_z) \boldsymbol{\rho} \mathbf{u}_t + \frac{1}{2} \mathbf{u}^T (\mathbf{M}_y^{\mu} + \mathbf{M}_z^{\mu}) \mathbf{u} \tag{50}$$

where

$$\mathbf{M}_y^{\mu} = (\mathbf{D}_y \otimes \mathbf{I}_z)^T \boldsymbol{\mu} \left(\mathbf{H}_y \otimes \mathbf{H}_z \right) (\mathbf{D}_y \otimes \mathbf{I}_z) + (\mathbf{I}_y \otimes \mathbf{H}_z) \mathbf{R}_y^{\mu}, \tag{51}$$

$$\mathbf{M}_z^{\mu} = (\mathbf{I}_y \otimes \mathbf{D}_z)^T \boldsymbol{\mu} \left(\mathbf{H}_y \otimes \mathbf{H}_z \right) (\mathbf{I}_y \otimes \mathbf{D}_z) + (\mathbf{H}_y \otimes \mathbf{I}_z) \mathbf{R}_z^{\mu}, \tag{52}$$

and the discrete total mechanical energy $\mathbf{E} = ||\mathbf{u}||_E^2$ is the sum of the discrete kinetic and strain energy.

To obtain a semidiscrete energy estimate, we again assume homogeneous boundary conditions (as in section 3, see also Appendix A), multiply equation (38) by $\mathbf{u}_t^T(\mathbf{H}_y \otimes \mathbf{H}_z)$ and add the transpose

$$\frac{\mathrm{d}}{\mathrm{d}t}\left(\frac{1}{2}\mathbf{u}_t^T(\mathbf{H}_y \otimes \mathbf{H}_z)\rho\mathbf{u}_t + +\frac{1}{2}\mathbf{u}^T(\mathbf{M}_y^\mu + \mathbf{M}_z^\mu)\mathbf{u}\right) = (\mathbf{u}_t)_f^T[\boldsymbol{\mu}(\mathbf{B}_y\mathbf{S}_y \otimes \mathbf{H}_z)\mathbf{u}]_f + (\mathbf{u}_t)_r^T[\boldsymbol{\mu}(\mathbf{B}_y\mathbf{S}_y \otimes \mathbf{H}_z)\mathbf{u}]_r + \\ + (\mathbf{u}_t)_s^T[\boldsymbol{\mu}(\mathbf{H}_y \otimes \mathbf{B}_z\mathbf{S}_z)\mathbf{u}]_s + (\mathbf{u}_t)_d^T[\boldsymbol{\mu}(\mathbf{H}_y \otimes \mathbf{B}_z\mathbf{S}_z)\mathbf{u}]_d + \\ + BT_\mathrm{f} + BT_\mathrm{r} + BT_\mathrm{s} + BT_\mathrm{d} \tag{53}$$

where

$$BT_f = \alpha_f(\mathbf{u}_t)_f^T\boldsymbol{\mu}_f\mathbf{H}_z\left(\mathbf{u}_f - \mathbf{g}_f\right) + \beta(\mathbf{u}_t)^T[\boldsymbol{\mu}\mathbf{B}_y\mathbf{S}_y \otimes \mathbf{H}_z)]^T\tilde{E}_f\left(\mathbf{u}_f - \mathbf{g}_f\right), \tag{54}$$

$$BT_r = \alpha_r(\mathbf{u}_t)_r^T\boldsymbol{\mu}_r\mathbf{H}_z\left(\mathbf{u}_r - \mathbf{g}_r\right) + \beta(\mathbf{u}_t)^T[\boldsymbol{\mu}(\mathbf{B}_y\mathbf{S}_y \otimes \mathbf{H}_z)]^T\tilde{E}_r\left(\mathbf{u}_r - \mathbf{g}_r\right), \tag{55}$$

$$BT_s = \alpha_s(\mathbf{u}_t)_s^T\left([\boldsymbol{\mu}\left(\mathbf{H}_y \otimes \mathbf{B}_z\mathbf{S}_z\right)\mathbf{u}]_s + \mathbf{g}_s\right], \tag{56}$$

$$BT_d = \alpha_d(\mathbf{u}_t)_d^T\left([\boldsymbol{\mu}\left(\mathbf{H}_y \otimes \mathbf{B}_z\mathbf{S}_z\right)\mathbf{u}]_d - \mathbf{g}_d\right). \tag{57}$$

Equation (53) represents the discrete analog of equation (31), where the left-hand side is the time derivative of the total mechanical energy. The first four terms on the right mimic the terms on the right of the continuous energy estimate (31) after integrating by parts. The remaining boundary terms BT, defined in equations (54)–(57), are the contributions from the SAT penalty vectors $\mathbf{p}_{f,r,s,d}$ obtained from enforcing the boundary conditions weakly. We prove in Appendix B that that energy is conserved or dissipated under the conditions $\alpha_s = \alpha_d = -1, \beta = 1$, and $\alpha_f, \alpha_r \leq -13/h_y$. Thus, (38) defines a second-order accurate, strictly stable discretization to the initial boundary value problem (26)–(30). These properties ensure that numerical solutions obtained by the discretization will converge to the true solution under mesh refinement.

6. Frictional Framework

Because our eventual goal in this work is to study how sedimentary basins affect general characteristics of the earthquake cycle, rather than resolving details of wave propagation during dynamic rupture, we adopt a quasi-dynamic modeling framework in which inertial effects are approximated with a radiation-damping term when balancing frictional resistance with shear tractions exerted by the elastic medium on the fault [*Rice*, 1993]. This means that we only need to solve the equations of static equilibrium in the medium.

Spatial discretizations obtained by studying the dynamic counterpart have been used to solve steady state problems in fluid dynamics [*Nordström et al.*, 2007; *Eriksson and Nordström*, 2009; *Hicken and Zingg*, 2011]. In a similar manner, we drop inertial terms from the elastic wave equation (26) to obtain

$$0 = \frac{\partial}{\partial y}\left(\mu\frac{\partial u}{\partial y}\right) + \frac{\partial}{\partial z}\left(\mu\frac{\partial u}{\partial z}\right), \quad (y,z) \in [0, L_y] \times [0, L_z]. \tag{58}$$

The corresponding discretization of (58) is given by the right-hand side of (38):

$$0 = \mathbf{D}_{2y}^\mu\mathbf{u} + \mathbf{D}_{2z}^\mu\mathbf{u} + \mathbf{p}_f + \mathbf{p}_r + \mathbf{p}_s + \mathbf{p}_d \tag{59}$$

where the SAT vectors $\mathbf{p}_{f,r,s,d}$ remain identical to those given in equations (43)–(46). The fault ($y = 0$, see Figure 2) is governed by rate-and-state friction [*Dieterich*, 1979a; *Ruina*, 1983; *Marone*, 1998]. The shear stress, $\tau = \mu\frac{\partial u}{\partial y}\Big|_{y=0}$, is set equal to fault strength:

$$\tau = F(V, \psi) \tag{60}$$

where fault strength F is normal stress σ_n times the friction coefficient f. In the rate-and-state framework, the fault strength is a function of slip velocity

$$V(z,t) = \frac{\partial u}{\partial t}\Big|_{y=0^+} - \frac{\partial u}{\partial t}\Big|_{y=0^-} = 2\frac{\partial u}{\partial t}\Big|_{y=0^+} \tag{61}$$

and a state variable ψ in the following form:

$$F(V,\psi) = a\sigma_n \sinh^{-1}\left(\frac{V}{2V_0}e^{\frac{\psi}{a}}\right) \tag{62}$$

where ψ undergoes its own time evolution

$$\frac{d\psi}{dt} = G(V,\psi). \tag{63}$$

While there are other forms for state variable evolution, we have chosen to use the aging law [*Marone*, 1998]

$$G(V,\psi) = \frac{bV_0}{D_c}\left(e^{\frac{f_0-\psi}{b}} - \frac{V}{V_0}\right), \tag{64}$$

where state can evolve in the absence of slip and may therefore be more appropriate for models accounting for the period of interseismic loading. Here f_0 is a reference friction coefficient for steady sliding at slip velocity V_0, a and b are dimensionless parameters characterizing the direct and state evolution effects, respectively, and D_c is the state evolution distance.

The analysis for stability of steady frictional sliding described by equations (60) and (62) has been done by *Ruina* [1983], *Rice and Ruina* [1983], *Gu et al.* [1984], *Ranjith and Rice* [1998], and *Rice et al.* [2001]. In the case of antiplane perturbations from steady sliding between identical solids, instability occurs for wave numbers below a critical wave number k_{cr}, which in the quasi-static limit is

$$k_{cr} = \frac{2(b-a)\sigma_n}{\mu D_c}. \tag{65}$$

This analysis has important consequences on the numerical discretization because it defines a critical wavelength:

$$h^* = \frac{2\pi}{k_{cr}} = \frac{\pi\mu D_c}{\sigma_n(b-a)}, \tag{66}$$

which must be well resolved by the grid to ensure accuracy of the numerical solution [*Rice*, 1993]. Note that other authors [*Rice*, 1993; *Lapusta et al.*, 2000; *Kaneko et al.*, 2011] employ a slightly different dimensionless prefactor when defining h^*, based on the particular numerical discretization technique.

It is essential to resolve not only the nucleation zone but also the region of rapid strength degradation immediately behind the tip of a propagating rupture. The latter is typically much smaller than h^* and involves the rate-and-state parameters a and b in a different manner. *Ampuero and Rubin* [2008] show that under many conditions, this characteristic length scale for the aging law can be expressed as

$$L_b = \mu D_c/(\sigma_n b). \tag{67}$$

We later ensure that both h^* and L_b are adequately resolved in our simulations.

7. Time-Stepping Method

To evolve the system in time we solve the static elasticity equation (58) (with discretization (59)) with time-dependent boundary conditions defined in section 4. The boundary condition at the fault is given by imposing the slip obtained by enforcing friction, as detailed below. The system is loaded at the remote boundary $y = L_y$ with a displacement boundary condition at rate $V_p/2$, with V_p on the order of 35 mm/a. Thus, the boundary conditions are given by

$$g_f(z,t) = \Delta u(z,t)/2 \tag{68}$$

$$g_s(y,t) = 0, \tag{69}$$

$$g_d(y,t) = 0, \tag{70}$$

$$g_r(z,t) = V_p t/2. \tag{71}$$

The radiation damping approximation of inertial effects allows us to express shear stress on the fault as

$$\tau = \tau_{qs} - \eta V \tag{72}$$

in which $\tau_{qs} = \mu \frac{\partial u}{\partial y}\Big|_{y=0}$ is the shear stress obtained from solving the quasi-static equations and $\eta = \mu/(2c_s)$ is half the shear-wave impedance. Equating τ with the fault strength yields the condition

$$\tau_{qs} - \eta V = F(V, \psi). \tag{73}$$

In the following time-stepping algorithm, the fields refer to their discrete counterparts. The algorithm is written generally in forward Euler form in equations (77)–(78), but we use MATLAB's explicit, fourth-order Runge–Kutta solver ode45 that provides error estimation and thus adaptive selection of time steps. Taking slip Δu^n and state ψ^n as known at time t^n, the time-stepping algorithm is as follows:

1. Use Δu^n to set the displacement boundary condition at the fault:

$$g_f(z, t^n) = \Delta u^n/2 \tag{74}$$

   and, along with the remaining boundary conditions set by (68)–(71), solve the linear system (59) to obtain the displacement field $u(y, z, t^n)$.
2. Compute the shear stress component at the fault:

$$\tau_{qs}^n = \mu \frac{\partial u^n}{\partial y}\Big|_{y=0}. \tag{75}$$

3. Equate the shear stress at fault with the fault strength:

$$\tau_{qs}^n - \eta V^n = F(V^n, \psi^n) \tag{76}$$

   and solve for slip velocity V^n (a nonlinear equation solved through a safe-guarded Newton method).
4. Update state ψ and slip Δu on the fault by explicitly integrating with the now known slip velocity:

$$\Delta u^{n+1} = \Delta u^n + \Delta t V^n, \tag{77}$$

$$\psi^{n+1} = \psi^n + \Delta t G(V^n, \psi^n) \tag{78}$$

   and return to step 1.

The time scale governing state evolution in equation (78) is $\sim D_c/V$. Because slip velocity V is close to zero during the interseismic period, time steps can be large until an event begins to nucleate at which point the time step decreases appropriately in order to fully resolve quasi-dynamic rupture.

8. Two-Dimensional Convergence Tests

We next verify the accuracy and stability of our numerical method through rigorous convergence tests. While the governing equations are nonlinear, we can still construct an exact solution that permits us to quantify error as a function of grid spacing. The specific procedure we employ is known as the method of manufactured solutions [*Roache*, 1998]. We first write down some arbitrary displacement field $u^*(y, z, t)$. By itself, this will not necessarily satisfy the governing equations and boundary conditions. However, any differences that arise in the equations are then added as boundary data and source terms. Thus, we manufacture a solution which satisfies the (58) with a source term (which can be physically interpreted as a body force) then use the known manufactured solution to set the boundary data at each time step. As outlined in the time-stepping algorithm in section 7, the boundary data at the fault are updated at each time step by computing the slip velocity obtained by equating shear stress with fault strength. The state variable is also updated at each time step, so we must add another source term to the state evolution equation.

The manufactured solution u^* is constructed to mimic the behavior we expect to see in nature, where the fault creeps steadily at depth at approximately V_p and the fault near the surface slipping almost entirely

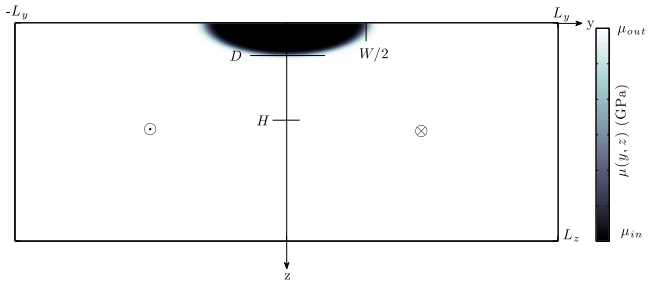

Figure 3. Material properties for our 2-D problems. The sedimentary basin of width W and depth D is idealized as a semiellipse. The shear modulus increases smoothly from a small value within the basin, μ_{in}, to a reference value μ_{out} outside the basin, over a short distance at the basin edges. H is the seismogenic depth.

during brief episodic rupture events. Letting δ denote the amount of slip in each rupture, we manufacture the solution

$$u^*(y,z,t) = \frac{\delta}{2}K(t)\phi(y,z) + \frac{V_p}{2}t\left[1-\phi(y,z)\right] + \frac{\tau^\infty}{\mu(L_y,z)}y, \quad (y,z)\in[0,L_y]\times[0,L_z], \quad t\geq 0 \tag{79}$$

where fields marked with an * refer to the exact solution. The spatial dependence is defined by the dimensionless function

$$\phi(y,z) = \frac{H(H+y)}{(H+y)^2+z^2}, \tag{80}$$

in which H plays the role of the locking (or seismogenic) depth and $0 \leq \phi(0,z) \leq 1$. As we expect the majority of slip to occur near Earth's surface $z=0$, $\phi(y,z)$ is constructed so that at the fault $y=0$ it takes the form of a normalized Lorentzian distribution:

$$\phi(0,z) = \frac{H^2}{H^2+z^2}. \tag{81}$$

The time dependence $K(t)$ for the manufactured solution is chosen so that the system undergoes an interseismic period of slow loading at the plate rate V_p before transitioning into a short coseismic period in which rupture occurs with slip velocity increasing over many orders of magnitude. For the particular form of $K(t)$ we take

$$K(t) = \frac{1}{\pi}\left[\tan^{-1}\left(\frac{t-\bar{t}}{t_w}\right)+\frac{\pi}{2}\right] + \frac{V_{\text{min}}}{\delta}t, \geq 0 \tag{82}$$

where parameter t_w defines an event duration, $\bar{t}$ defines when the event occurs, and V_{min} defines a minimum slip velocity. If L_y is taken sufficiently large, τ^∞ defines the remote stress.

We choose a semiellipse to idealize the geometry of the sedimentary basin, so that the shear modulus varies smoothly within the domain:

$$\mu(y,z) = \frac{\mu_{\text{out}}-\mu_{\text{in}}}{2}\left[\tanh\left(\frac{r-\bar{r}}{r_w}\right)+1\right]+\mu_{\text{in}}, \quad (y,z)\in[-L_y,L_y]\times[0,L_z], \tag{83}$$

where $r = y^2 + c^2z^2$, for parameter c, the ratio between major and minor axes of the ellipse (Figure 3). For basin of width W and depth D, $c = (W/2)/D$. The shear modulus $\mu(y,z)$ assumes a low, constant value of μ_{in} inside the sedimentary basin defined by an ellipse. At $r=\bar{r}$, μ increases smoothly with increasing r over a short width defined by r_w to a new value μ_{out} outside of the basin where the material is stiffer.

One can check that $u^*(y,z,t)$ in (79) solves equation (58) with a source term in the domain. The initial conditions and boundary data are also defined by $u^*(y,z,t)$. The slip along the fault is given by

$$\Delta u^*(z,t) = 2u^*(0,z) = \delta K(t)\phi(0,z) + V_p t\left[1-\phi(0,z)\right] \tag{84}$$

and the shear stress from quasi-static equilibrium at the fault is given by

$$\tau^*_{\text{qs}}(z,t) = \mu(0,z)\left.\frac{\partial u^*}{\partial y}\right|_{y=0} = \mu(0,z)\left[\frac{\delta}{2}K(t)\frac{\partial\phi}{\partial y}(0,z) - \frac{V_p}{2}t\frac{\partial\phi}{\partial y}(0,z) + \frac{\tau^\infty}{\mu(L_y,z)}\right]. \tag{85}$$

Table 1. Model Parameters Used for the Manufactured Solution[a]

Parameter	Value
L_y	40 km
L_z	40 km
H	8 km
W	24 km
D	6 km
$\bar{r}$	$(W/2)^2$ km
r_w	20 km
μ_{in}	18 GPa
μ_{out}	24 GPa
ρ_{in}	2600 kg/m^3
ρ_{out}	3000 kg/m^3
σ_n	50 MPa
a	0.015
b	0.02
D_c	0.2 m
V_p	10^{-9} m/s
V_0	10^{-6} m/s
f_0	0.6
V_{min}	10^{-12} m/s
t_w	10 s
$\bar{t}$	35 a
t_f	70 a
τ^∞	31.73 MPa

[a]We take as the remote stress $\tau^\infty = \sigma_n a \sinh^{-1}(\frac{V_p}{2V_0} e^{\psi_p/a})$, where $\psi_p = f_0 - b\ln(V_p/V_0)$ corresponds to steady state value at sliding velocity equal to the plate rate V_p.

The slip velocity is

$$V^*(z,t) = 2\frac{\partial u^*}{\partial t}|_{y=0} = \delta K'(t)\phi(0,z) + V_p\,[1-\phi(0,z)]\,. \tag{86}$$

The conditions

$$\frac{\delta}{2}F'(t) \geq 0, \quad \frac{\mu_{\text{out}}}{H}\frac{V_p}{2}t_f \leq \tau^\infty, \tag{87}$$

where t_f is the final time of simulation ensure that τ^* and V^* share the same sign (and are both positive), which is a necessary condition for well posedness of this problem [*Kozdon et al.*, 2011].

We expect that slip near the surface catches up with slip at depth, which is approximately achieved by setting $\delta = V_p\bar{t}/2 - V_{\text{min}}\bar{t}$. Inserting τ^* and V^* into equation (73) allows us to solve for ψ^*. Thus, the manufactured solution requires adding a source term to the state evolution law:

$$\frac{d\psi}{dt} = G(V,\psi) + s(z,t) \tag{88}$$

where the source term $s(z,t)$ is solved for by substituting into equation (88) the exact solutions $\psi^*(z,t)$ and $V^*(z,t)$.

The parameters used for this solution and associated convergence tests are given in Table 1. Note that we assume depth independent values of the frictional parameters a and b, which differs from our application problem in section 8. Properties of the solution are shown in Figures 4 and 5.

In discretizing the computational domain we take $L_y = L_z$ and $N := N_z = N_y$. As described in section 6, our grid spacing h must be small enough to resolve the process zone $L_b = \min(\mu D_c)/(\sigma_n b)$ where the minimum is taken over the fault. For the parameters we have chosen for the manufactured solution, $L_b \approx 3.6$ km, and all convergence test simulations resolve L_b with a minimum of five grid points. We time step using MATLAB's ode45 solver with a relative tolerance of 10^{-9}.

Table 2 lists the relative error between the exact solution and numerical approximation in both the discrete H norm defined by (49) and a modified discrete energy norm at the end of the simulation $t = t_f$. The relative error in the discrete H norm is given by

$$\text{Error}_H(h) = \frac{||\mathbf{u}^* - \mathbf{u}||_H}{||\mathbf{u}^*||_H} \tag{89}$$

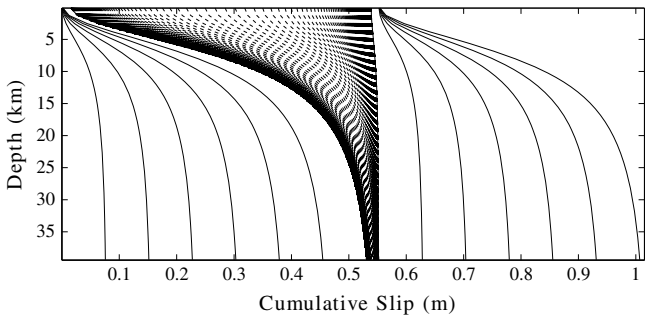

Figure 4. Slip profiles of the manufactured solution plotted every 5 a (solid) during the interseismic period ($V \leq 1$ mm/s) and every 5 s (dashed) during the quasidynamic period. During the interseismic period, the fault remains relatively locked near the surface while creeping at depth. Once the event nucleates, slip near the surface catches up with slip at depth.

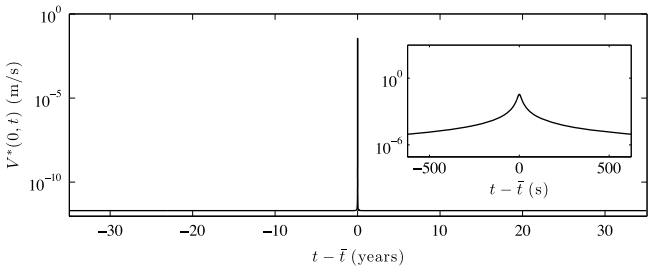

Figure 5. (a) Surface slip velocity over entire simulation period of 70 years, where values range over 10 orders of magnitude. (b) Zoom of surface slip velocity in the 20 min interval surrounding the quasi-dynamic rupture event.

where $\mathbf{u}^*$ is the exact solution evaluated at the spatial grid used to obtain the discrete approximation $\mathbf{u}$. We also compute the error made using the energy norm (50) but modified for the quasi-static problem by neglecting kinetic energy. Thus, the energy norm is

$$||\mathbf{u}||_E^2 = \frac{1}{2}\mathbf{u}^T(\mathbf{M}_y^\mu + \mathbf{M}_z^\mu)\mathbf{u} \tag{90}$$

with associated relative error given by

$$\text{Error}_E(h) = \frac{||\mathbf{u}^* - \mathbf{u}||_E}{||\mathbf{u}^*||_E}. \tag{91}$$

Figure 6 shows that in both the discrete H and the energy norm, we achieve second-order convergence, as expected. For any fixed grid spacing h, the error at time t for a finite time simulation $0 \leq t \leq T$ will be bounded by an $O(h^2)$ constant [*Gustafsson et al.*, 1995]. There remains the question of whether error will continue to increase over multiple earthquakes. In the next section we simulate earthquakes sequences, in which the solution always enters a limit cycle composed of periodic sequences of earthquakes. We speculate that for an exact time-stepping method, the spatial error associated with the semidiscrete equations also enters a related limit cycle, rather than continuing to grow during each cycle. That being said, errors from time integration might ultimately begin to accumulate over multiple cycles, causing the overall error to grow in time. However, the simulations presented in this work require only ∼10 events to spin up to the limit cycle, and after this spin-up period the numerical solutions show negligible changes between subsequent cycles.

9. Earthquake Cycles in Basins

Having verified in the previous section that our numerical method furnishes a solution which converges to the true solution under mesh refinement, we apply the method to study how sedimentary basins influence the earthquake cycle. Frictional properties are depth dependent (Table 3 and Figure 7). The fault transitions from velocity-weakening to velocity-strengthening over a finite distance, beginning at seismogenic depth $H = 12$ km. Our specific focus is on the role of elastic heterogeneity, and we therefore use the same velocity-weakening properties within the basin as below it, rather than making the section of the fault within the basin velocity-strengthening. In the same spirit, we use a constant normal stress of $\sigma_n = 50$ MPa at all depths. Future work should explore more realistic depth variations of frictional properties and normal stress and determine their contribution to complexity in earthquake sequences, but such an effort is beyond the scope of this initial work.

Table 2. Relative Error in the Discrete H and Energy Norms[a]

N	$\text{Error}_H(h)$	Rate	$\text{Error}_{\tilde{E}}(h)$	Rate
2^6	1.847×10^{-5}	–	4.697×10^{-4}	–
2^7	5.602×10^{-6}	1.721	1.161×10^{-4}	2.016
2^8	1.336×10^{-6}	2.068	2.886×10^{-5}	2.008
2^9	3.471×10^{-7}	1.945	7.191×10^{-6}	2.005
2^{10}	8.436×10^{-8}	2.039	1.794×10^{-6}	2.003

[a]The rate of convergence approaches 2, as expected for a method with second-order accuracy.

To constrain the shear modulus μ within and outside the basin, we queried the Southern California Earthquake Center (SCEC) Community Velocity Model (CVM-H v. 11.9.1, see http://scec.usc.edu/scecpedia/CVM-H, *Tape et al.* [2009]) at depth at various regions in Southern California. Average values of μ in the upper ∼5 km in basin regions along the San Andreas Fault are roughly between 10

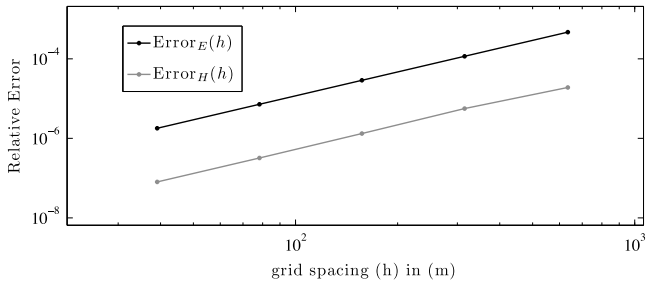

Figure 6. Relative error in the discrete H and energy norms as a function of grid spacing h. The slope of the line reflects the second-order accuracy of the method.

and 20 GPa (and even lower near Earth's surface) and increase with depth before leveling off to 35–40 GPa around 5–10 km depth (Figure 8a). As also seen in the same figure, outside of basin regions μ assumes average values closer to 31–35 GPa in the upper ~5 km, with a representative value of 34 GPa (Figure 8b).

We conduct a parameter study by varying basin depth D and basin shear modulus μ_{in} with all other parameters held fixed. The two basin depths D considered are 4 and 8 km, corresponding to 1/3 and 2/3 times the seismogenic depth H, respectively. The shear modulus outside the basin is fixed at μ_{out} = 36 GPa, and μ_{in} assumes values of either 8 or 16 GPa. All simulations are done with state evolution distance D_c = 8 mm, which is artificially enhanced by several orders of magnitude from laboratory values. The process zone length scale L_b is resolved with approximately five grid points for all simulations. While it is desirable to use smaller values of D_c to have smaller nucleation zones, it is beyond our current computational capabilities. We also verify in Appendix C that our artificial truncation of the computational domain has minimal influence on the results.

The initial conditions, corresponding to steady creep at V_p along the entire fault, are

$$V(z,0) = V_p, \tag{92}$$

$$\Delta u(z,0) = 0, \tag{93}$$

$$\tau(z,0) = \tau^{\infty}, \tag{94}$$

$$\psi(z,0) = a \ln\left[\frac{2V_0}{V_p}\sinh\left(\frac{\tau^{\infty} - \eta V_p}{\sigma_n a}\right)\right], \tag{95}$$

where the parameters for these simulations are given in Table 3. However, after a few cycles, the system evolves into event sequences that appear to be independent of these initial conditions. The boundary data are

$$g_f(z,t) = \frac{1}{2}\Delta u(z,t), \tag{96}$$

$$g_s(y,t) = g_d(y,t) = 0, \tag{97}$$

$$g_r(z,t) = \frac{\tau^{\infty} L_y}{\mu(L_y,z)} + \frac{V_p}{2}t. \tag{98}$$

Our primary results are presented in two comparative figures (Figures 9 and 10), which show snapshots of cumulative slip for various parameter values. Slip is plotted with a solid line every 5 a during the interseismic

Table 3. Parameters Used in the Earthquake Cycle Simulations[a]

Parameter	Value
L_y	24 km
L_z	24 km
W	24 km
D	variable
H	12 km
$\bar{r}$	$(W/2)^2$ km
r_w	$1 + (W/2)/D$ km
μ_{in}	variable
μ_{out}	36 GPa
ρ_{in}	variable
ρ_{out}	2800 kg/m^3
σ_n	50 MPa
a	0.015
b	depth variable
D_c	8 mm
V_p	10^{-9} m/s
V_0	10^{-6} m/s
f_0	0.6
τ^{∞}	24.82 MPa

[a]We take as the remote stress $\tau^{\infty} = \sigma_n a \sinh^{-1}(\frac{V_p}{2V_0} e^{f_0/a})$.

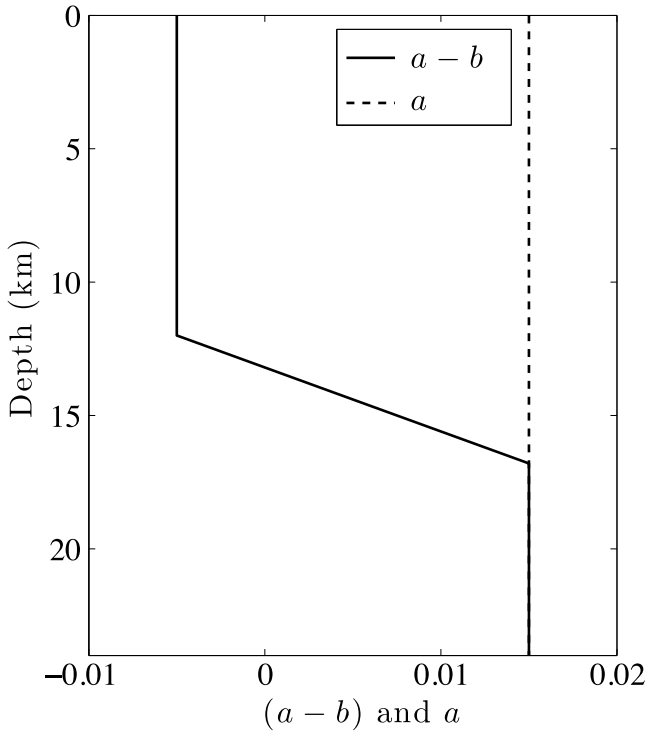

Figure 7. Depth dependence of frictional parameters a and $a - b$. Events nucleate in the seismogenic region above the seismogenic depth $H = 12$ km (for these simulations), where $a-b < 0$ so that the fault is velocity weakening. It transitions to velocity strengthening at depth where $a - b > 0$.

period, which we define as max(V) $\leq$ 1 mm/s and plotted with a dashed line every 1 s during a quasi-dynamic event in which max(V) > 1 mm/s, where the max is taken over the entire fault.

In the first simulation (Figure 9), we set $\mu_{in} = 8$ GPa and $\rho_{in} = 2000$ kg/m^3 and vary basin depth D. (Note that the density ρ enters only through the radiation-damping term in the calculation of slip velocity at the fault from equation (73) and is not present in the equilibrium equation (58).) Figure 9a is the reference case for no basin. Interseismic creep extends up to about 8–9 km from the surface. Events nucleate periodically in the seismogenic zone at a depth of about 10 km, accumulating approximately 2–3 m of slip during each event. Figure 9b shows the results for a 4 km deep basin ($D = H/3$), with all other parameters unchanged. Events nucleate in the seismogenic region at about the same depth. Two types of rupture occur in succession,

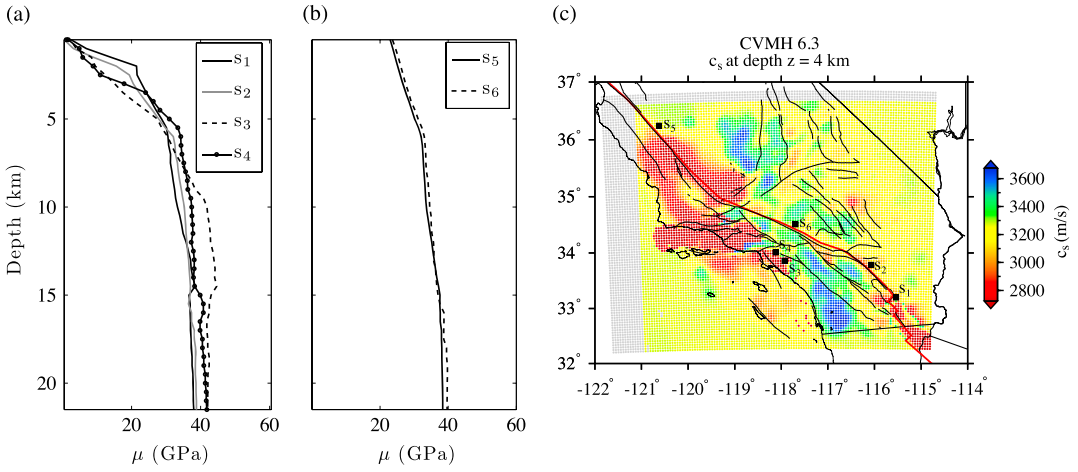

Figure 8. Profiles of shear modulus μ from the SCEC CVM-H at locations both (a) within and (b) outside sedimentary basins in the Los Angeles and Salton Sea areas. (c) Locations shown, figure courtesy of C. Tape.

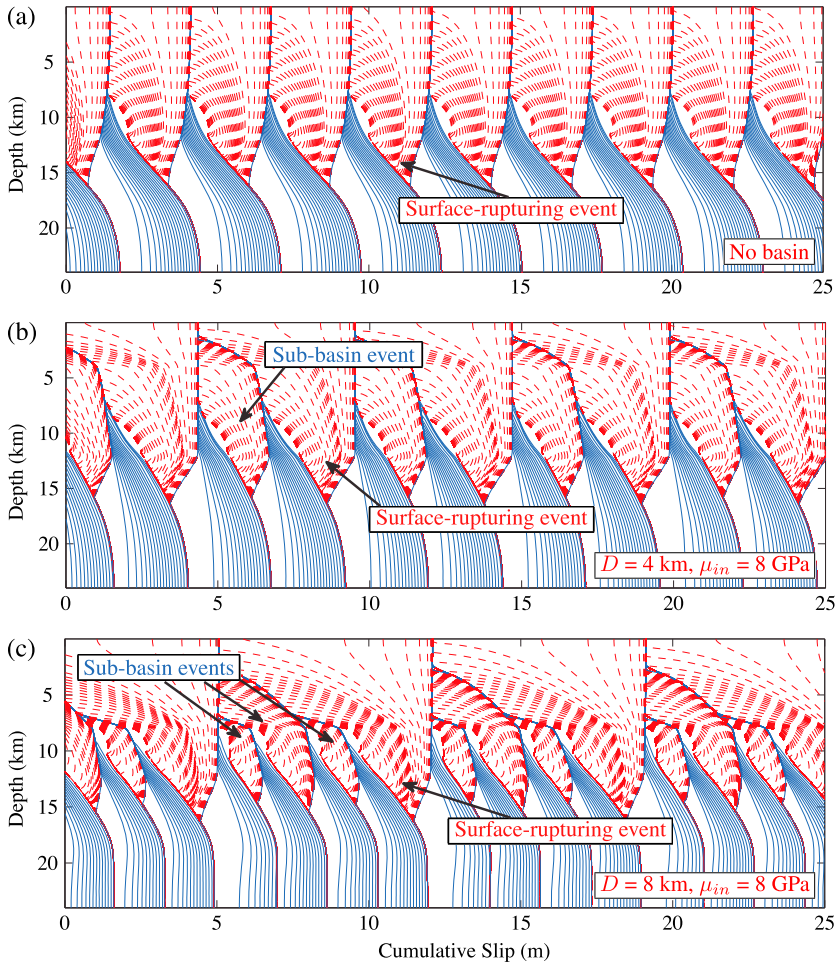

Figure 9. Snapshots of cumulative slip profiles for D_c = 8 mm and μ_{in} = 8 GPa. Solid blue profiles plotted at 5-a intervals during interseismic period when max(V) $\leq$ 1 mm/s, dashed red profiles plotted at 1 s intervals during quasi-dynamic rupture. (a) No basin. (b) Four kilometer deep basin ($D = H/3$). (c) Eight kilometer deep basin ($D = 2H/3$).

subbasin and surface-rupturing events. Subbasin ruptures produce several meters of slip, principally at depths greater than about 3 km. In these events, the sedimentary basin prevents rupture penetration to the surface, as evident from the sharp contours in the slip profiles near the lower edge of the basin. As discussed later in more detail, the subbasin event leaves a stress concentration at the bottom of the basin. With the help of this stress concentration, the next event penetrates through the basin to the surface in a surface-rupturing event. The stress concentration at the basin bottom is relieved, and the next event is again a subbasin one. This alternating sequence of subbasin and surface-rupturing events occurs periodically.

Increasing the basin depth to 8 km, ($D = 2H/3$, Figure 9c), the number of subbasin events preceding a surface-rupturing event increases from one to three. The first and third subbasin events barely penetrate past the basin depth, whereas the second subbasin event is able to penetrate farther although it is still unable to reach the surface. The subbasin events are smaller in extent and only introduce about 1–2 m of slip at depths near the edge of the basin.

We attribute the occurrence of different sized events to the elastic heterogeneity of our model. It is important to point out that variability in event size, in particular the emergence of small events, also occurs for faults in uniform half-spaces as the nucleation length h^* is decreased for fixed fault dimension [*Lapusta and Rice*, 2003]. A potential concern here is that the reduced shear modulus within the basin is decreasing h^* (see equation (66)), thereby permitting small earthquakes. However, at least for the shallow basin case (Figure 9b), nucleation occurs well outside the basin and it is thus unlikely that the basin directly influences the nucleation and early growth of the rupture. That case provides clear evidence that elastic heterogeneity

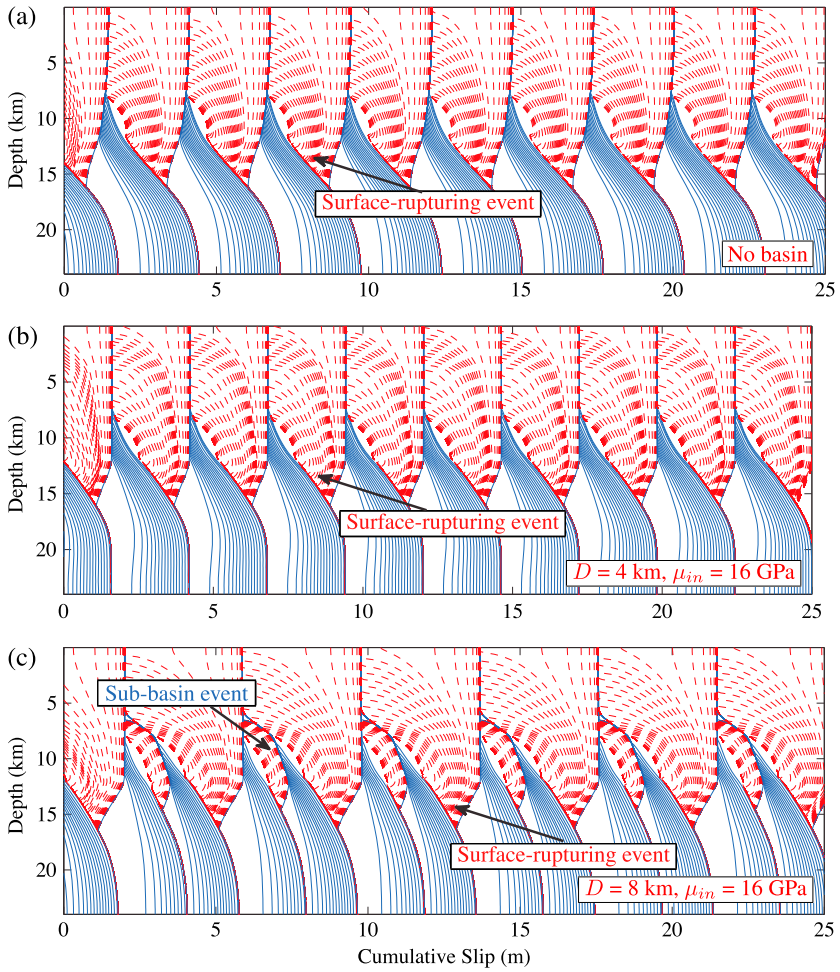

Figure 10. Snapshots of cumulative slip profiles for D_c = 8 mm and μ_{in} = 16 GPa. Solid blue profiles plotted at 5-a intervals during interseismic period when max(V) ≤ 1 mm/s, dashed red profiles plotted at 1 s intervals during quasi-dynamic rupture. (a) No basin. (b) Four kilometer deep basin ($D = H/3$). (c) Eight kilometer deep basin ($D = 2H/3$).

can, by itself, introduce complexity in earthquake sequences. The same is not true for the deeper basin case (Figure 9c), where accelerating creep in the nucleation zone extends into the lower part of the basin.

In Figure 10 we study the influence of basin sediment stiffness by setting $\mu_{in} = 16$ GPa and $\rho_{in} = 2560$ kg/m^3. Figure 10a is the reference case for no basin. While this case is identical to that shown in Figure 9a, we include it for ease of comparison. In contrast to the more compliant basin case shown in Figure 9b, the 4 km deep basin (Figure 10b) now has only minimal influence on the earthquake cycle, and all events break through to the surface. Subbasin events only emerge with a deeper basin in this case (Figure 10c).

We thus conclude from our limited parameter space study that subbasin events only emerge for sufficiently compliant and/or deep basins. A natural extension of this work would be to map out event sequence styles in the two-dimensional parameter space of basin size and rigidity contrast relative to the surrounding material.

Subbasin ruptures relieve some of the stress accumulated during interseismic loading, thus delaying the occurrence of surface-rupturing events. Recurrence intervals of surface-rupturing events, which are the only ones accessible through surface paleoseismic trenching studies, are therefore longer. To better understand the timing of surface-rupturing events, we plot surface slip velocity as a function of time for our simulations in Figure 11. For the simulations in Figure 9 with $\mu_{in} = 8$ GPa, the recurrence intervals are approximately 90, 150, and 220 years for $D = 0$, 4, and 8 km, respectively, as seen in Figure 11a. In this case the presence of a basin gives rise to subbasin events, which delay the occurrence of the surface-rupturing events. Figure 11b

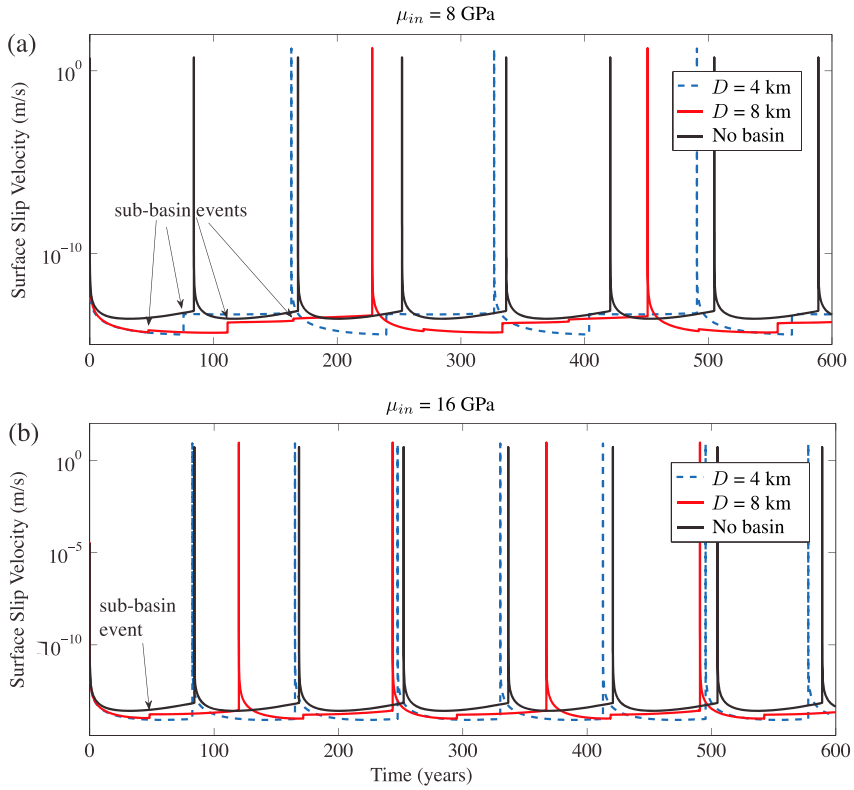

Figure 11. Surface slip velocity history, illustrating influence of basins on recurrence intervals of surface-rupturing events. Shown are results for three basin depths D (0, 4 km, and 8 km) for (a) μ_{in} = 8 GPa and (b) μ_{in} = 16 GPa.

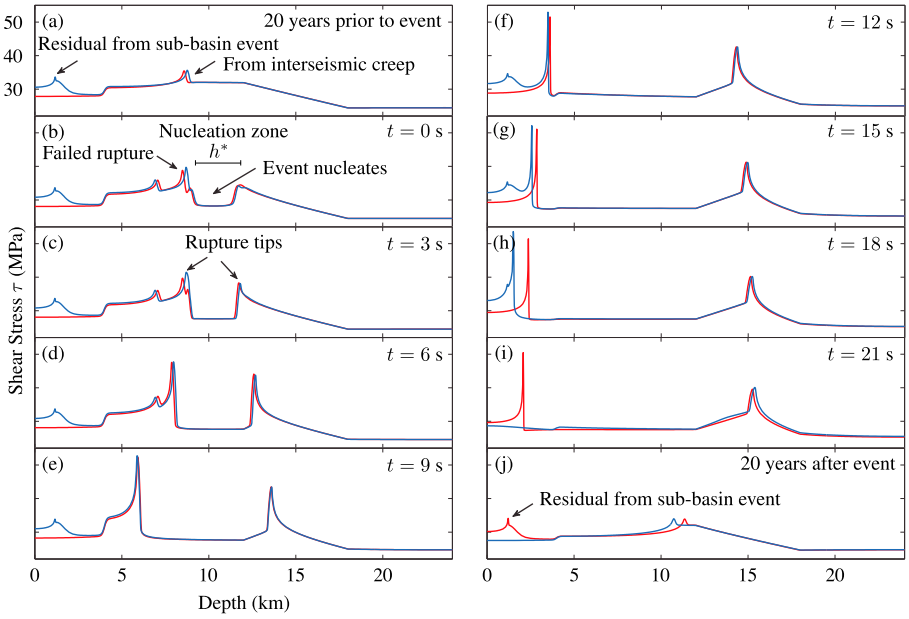

Figure 12. Comparison of shear stress (a) before, (b–i) during, and (j) after a subbasin event (red) and a surface-rupturing event (blue). The surface-rupturing event penetrates through the basin with the assistance of the residual stress concentration left by the subbasin rupture. Shown for D = 4 km ($D = H/3$), μ_{in} = 8 MPa (same as Figure 9b).

shows the surface slip velocity for μ_{in} = 16 GPa, and the recurrence interval is about 90, 90, and 120 years for D = 0, 4, and 8 km, respectively. The lack of difference between the D = 0 and 4 km cases is explained by the absence of subbasin events for the stiff, shallow basin case. For these parameter choices the recurrence interval of surface-rupturing events increases with increasing basin depth. Further parameter space studies are warranted to quantify the dependence of recurrence interval on basin properties, but they are beyond the scope of this work.

To further understand the emergence of subbasin ruptures, we examine in more detail the simulation shown in Figure 9b. In Figure 12 we compare the shear stress τ along the fault before and during subbasin and surface-rupturing events. The primary difference in prestress conditions is the stress concentration in the basin (at a few kilometers depth) that is left when a subbasin event fails to reach the surface. This feature is only present before a surface-rupturing event, as shown in Figure 12a (20 years before the events begin). Otherwise, the stress fields are nearly identical. Both have an additional stress concentration around 9 km depth due to interseismic creep extending slightly past the transition zone into the velocity-weakening zone. Another stress concentration, which can be seen in Figure 12b at around 8 km depth, emerges after a failed attempt to rupture.

Nucleation of both the subbasin and surface-rupturing events appears to be identical. Both begin around 10 km depth in a nucleation zone having width approximately equal to h^* (about 3 km in this case). The initial instability develops into a bilaterally expanding rupture (Figures 12c–12f). However, as shown in Figures 12g–12i, when the subbasin rupture reaches the sedimentary basin, the rupture slows down and arrests before reaching the surface. In contrast, the surface-rupturing event reaches the residual stress concentration left by the previous subbasin event and propagates all the way through the basin to the surface. Figure 12j shows the shear stress profiles 20 years after each event type, illustrating the residual stress concentration left by the subbasin rupture.

10. Summary and Discussion

We have developed an efficient numerical method for simulating earthquake sequences with a finite-difference discretization of the equations governing the off-fault material. While most current methods for earthquake cycles are based on a boundary integral or boundary element framework and are therefore limited to homogeneous elastic half-spaces, our method naturally handles heterogeneous material properties. The method can also be extended to incorporate off-fault inelastic response, as discussed by *Erickson and Dunham* [2012]. The volume discretization is obtained using finite difference operators satisfying a summation-by-parts (SBP) rule. The fault is governed by rate-and-state friction, and the system is loaded through a remote displacement boundary condition. Boundary conditions are enforced weakly at the edges of the computational domain through the simultaneous-approximation-term (SAT) method. The SBP-SAT framework leads to a semidiscretization of the dynamic problem which is provably strictly stable. We then disregard inertia in the momentum balance and instead employ the radiation-damping approximation. A natural next step would be to rigorously include inertial dynamics during the coseismic phase. Our time-stepping algorithm efficiently integrates the system through the interseismic period and quasi-dynamic rupture events. Although the equations are nonlinear and material properties are spatially variable, we manufactured an exact solution which we use to verify that our numerical method converges to the exact solution at the expected rate.

We then used our numerical method to study how the earthquake cycle is affected by the presence of a compliant sedimentary basin with elastic properties similar to those found in Southern California. The basin is represented by a semiellipse of reduced shear modulus. By varying basin depth and stiffness, we find that deep, compliant basins give rise to sequences of alternating subbasin and surface-rupturing events. The subbasin events are predominantly confined to depths at or below the basin depth (although some penetrate partially into the basin) and are much smaller than the surface-rupturing events. They do, however, delay the occurrence of the surface-rupturing events, which are consequently larger than in simulations lacking subbasin events. It is possible that a similar phenomenology of alternating subsurface and surface-rupturing events might occur in subduction zones, with most megathrust events stopping at the downdip limit of the accretionary prism and only a few breaking through to the trench like in the 2011 Tohoku-oki event. Additional investigations in an actual subduction zone geometry, and with realistic depth-dependent stresses and frictional properties, are needed.

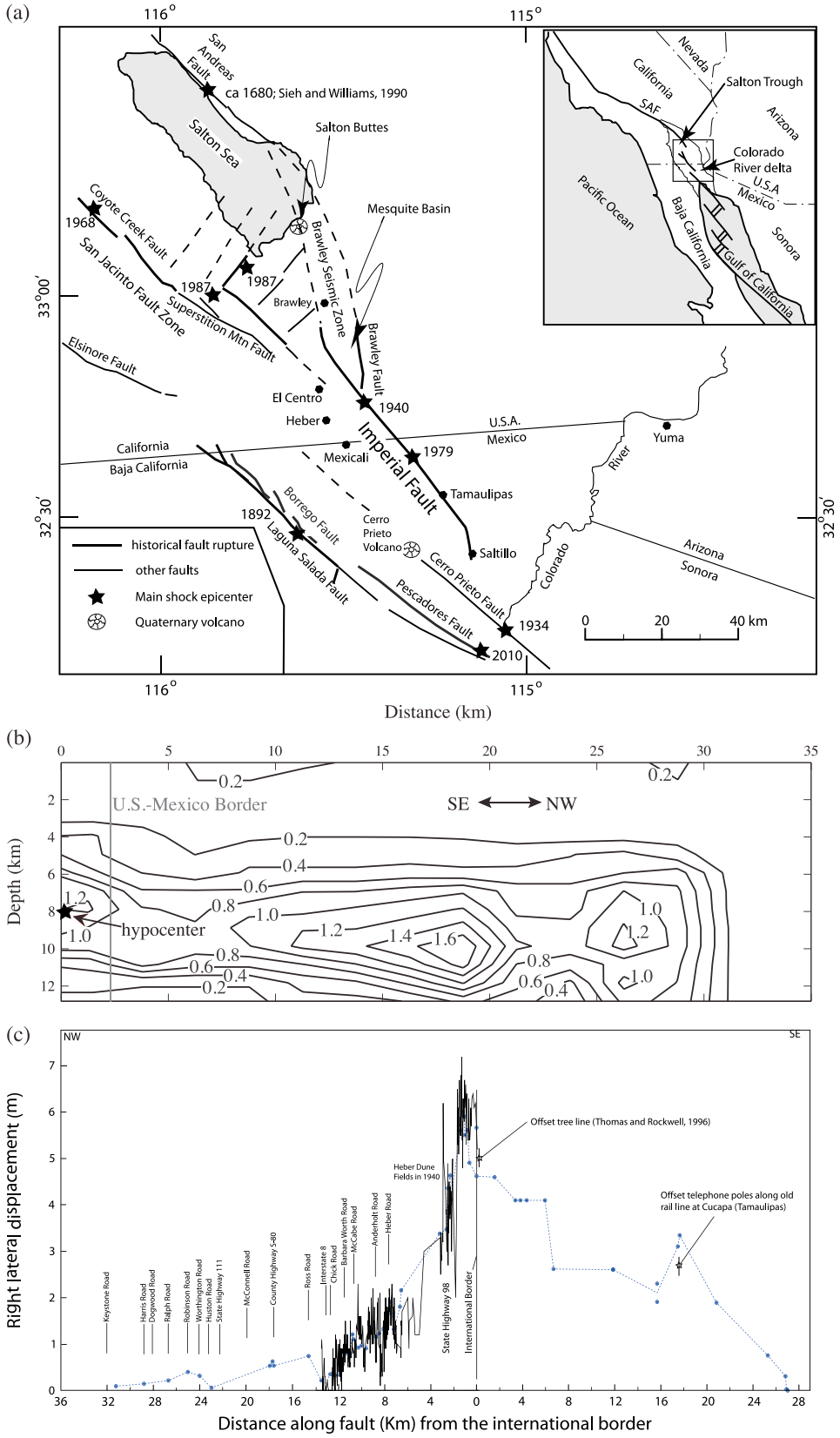

Figure 13. (a) Map of the Imperial Valley fault, from *Rockwell and Klinger* [2013]. (b) Slip distribution (m) for the 1979 event, as inferred by *Archuleta* [1984], from *Mai* [2014]. (c) Surface slip distribution in the 1940 event, from *Rockwell and Klinger* [2013].

Examination of surface velocity profiles during the interseismic periods before subbasin and surface-rupturing events (not shown) reveals nearly identical motions. Thus, geodetic measurements could not be used to predict rupture mode. This echoes the conclusions of *Lapusta and Rice* [2003] that the nucleation process of both small and large events is essentially the same. The ultimate extent of rupture is controlled instead by the stress conditions encountered by the growing rupture, which are set here by the past history of rupture as influenced by elastic heterogeneity.

It should be noted that *Lapusta and Rice* [2003] have shown that nonsurface rupturing events emerge in a homogeneous earthquake cycle model with sufficiently small nucleation size h^*. Since h^* is directly proportional to the shear modulus μ, the compliant basin materials reduce h^* near the surface, and one might worry that the smaller, subbasin events in our simulations arise simply from the reduced h^*. However, nucleation in our shallow ($D = 4$ km) simulations occurs well below the lower edge of the basin and in a manner that is effectively identical to nucleation in a homogeneous medium. The confinement of slip in subbasin events is thus caused by elastic heterogeneity. Simulations employing a smaller h^* than we have been able to use here will undoubtedly reveal even more complex earthquake sequences and a wider range of event sizes, but we suspect that the emergence of subbasin events due to elastic heterogeneity is a robust feature of this system in certain parts of parameter space.

The subbasin events seen in our simulations with a 4 km deep, compliant basin (Figure 9b) have slip distributions that are similar to several recent strike-slip events in having a shallow slip deficit. In our simulations, that deficit is ultimately relieved during a much larger event with extensive slip near and at the surface, rather than by shallow creep. The two most recent large events on the Imperial Fault (Figure 13a) offer a unique example of these two rupture styles. In the 1979 M_w 6.5 Imperial Valley earthquake, most slip occurred beneath a sedimentary layer approximately 4 km thick, reaching a maximum of 1.5–2 m at nearly 10 km depth [*Hartzell and Heaton*, 1983; *Archuleta*, 1984] (Figure 13b). This is quite different than the 1940 M_w 7.0 Imperial Valley event, which featured extensive surface slip [*Sharp et al.*, 1982]. The northern half of the 1940 rupture took place on the same section of fault as the 1979 event but with much more slip. In fact, a recent study by *Rockwell and Klinger* [2013] suggests an average of 5.5 m slip at the surface over the central section of the 1940 rupture near the U.S.-Mexico border, near the hypocenter of the 1979 event (Figure 13c). The patterns and amounts of slip in these earthquakes are somewhat similar to those shown in Figure 9b. We do point out that the Imperial Fault does creep near the surface [*Lyons et al.*, 2002], suggesting that the behavior observed in our simulations persists when the shallow fault surface is velocity strengthening.

If the behavior seen in our simulations is common in nature, then there are important implications for seismic hazard. Many faults overlain with sediments have minimal surface expression and, particularly in poorly studied regions of the world, can go unrecognized. The 2003 M_w 6.5 Bam, Iran, earthquake is one such example [*Talebian et al.*, 2004; *Fialko et al.*, 2005]. Yet as devastating as it was, there exists the possibility that subsequent events might be substantially larger. Further study is warranted to explore a wider range of frictional properties and more realistic depth dependence of normal stress, as well as the inelastic response of sediments [*Kaneko and Fialko*, 2011]. Nonetheless, our initial study offers one explanation for the shallow slip deficit that may help explain the behavior of faults that extend into sedimentary layers or basins but lack appreciable shallow aseismic creep.

Appendix A: Extension of the Homogeneous Boundary Data Assumption

For linear partial differential equations, the definition of well posedness means that the problem exhibits a unique solution depending continuously on the input (initial and boundary conditions, or possible source terms) of the problem. This last requirement means that small perturbations in the input data lead to small perturbations in the solution. This property is ensured if one can obtain an estimate for the solution $u(y, t)$ of equation (1) of the following form:

$$||u(\cdot, t)|| \leq \kappa e^{\zeta t} ||u_0(\cdot)|| \tag{A1}$$

for a suitable norm $||\cdot||$ and constants κ, ζ which are independent of the initial data (2)–(3) [*Gustafsson et al.*, 1995]. In the energy method, estimate (A1) follows from integration of (6)–(7), with $\kappa = 1$ and $\zeta = 0$ with the

suitable norm being the total mechanical energy of the system. In the discrete energy method, the discrete analog of estimate (A1) is

$$||\mathbf{u}||_h \leq \kappa_d e^{\zeta_d t}||\mathbf{u}_0||_h \tag{A2}$$

for a suitable discrete norm $||\cdot||_h$, grid function $\mathbf{u}$ and constants κ_d, ζ_d independent of $\mathbf{u}_0$ (and constants κ_d, ζ_d are, in general, different than κ, ζ obtained for the continuous problem). The definition of strict stability means that the growth rates in the energy estimates satisfy $\zeta_d \leq \zeta + O(h)$.

Estimate (A1) is expressed for a problem with homogeneous boundary data ($g_l = g_r = 0$) and no source terms; however, a similar estimate can be expressed in terms of all the (possibly inhomogeneous) data of the problem. In this work, we obtain estimates for the case of homogeneous boundary data and no source terms. This is for simplicity in the analysis only. One can always transform a problem like (1)–(5) with inhomogeneous boundary data to one with zero boundary data plus a source term. Duhamel's principle guarantees that if one can show the problem with no source function is well posed, then the problem with a source function will be well posed as well [*Gustafsson et al.*, 1995]. Thus, in our analysis in this work we always assume boundary data to be zero, for simplicity, with the understanding that the results extend to the problem with general boundary data.

Appendix B: Derivation of Penalty Parameters Through the Discrete Energy Method

The remaining operators defined in section 3 are

$$\mathbf{D} = \frac{1}{h}\begin{bmatrix} -1 & 1 & & & \\ -\frac{1}{2} & 0 & \frac{1}{2} & & \\ & \ddots & & & \\ & & -\frac{1}{2} & 0 & \frac{1}{2} \\ & & & -1 & 1 \end{bmatrix}$$

$$\mathbf{D}_2 = \frac{1}{h^2}\begin{bmatrix} 1 & -2 & 1 & & & & \\ 1 & -2 & 1 & & & & \\ & 1 & -2 & 1 & & & \\ & & \ddots & \ddots & \ddots & & \\ & & & 1 & -2 & 1 & \\ & & & & 1 & -2 & 1 \\ & & & & 1 & -2 & 1 \end{bmatrix}, \quad \mathbf{C}_2 = \begin{bmatrix} 0 & & & \\ & 1 & & \\ & & \ddots & \\ & & & 1 \\ & & & & 0 \end{bmatrix}.$$

Taking $\alpha_0 = -1$ and $\beta = 1$ in the 1-D semidiscrete energy estimate, equation (23) simplifies to

$$\frac{\mathrm{d}}{\mathrm{d}t}\left(\frac{1}{2}\mathbf{u}_t^T\mathbf{H}\rho\mathbf{u}_t + \frac{1}{2}\mathbf{u}^T\mathbf{M}^\mu\mathbf{u}\right) = \mathbf{u}_t^T[\alpha_1\mathbf{E}_N\boldsymbol{\mu} + \mathbf{E}_N\boldsymbol{\mu}\mathbf{BS} + (\mathbf{E}_N\boldsymbol{\mu}\mathbf{BS})^T]\mathbf{u} \tag{B1}$$

where we have taken $g_l = g_r = 0$ (done for analysis only, see Appendix A), and $\mathbf{E}_N = \mathbf{e}_N\mathbf{e}_N^T$ and $\mathbf{E}_0 = \mathbf{e}_0\mathbf{e}_0^T$. Thus, for a semidiscrete energy estimate, the matrix

$$\mathbf{A} := \alpha_1\mathbf{E}_N\boldsymbol{\mu} + \mathbf{E}_N\boldsymbol{\mu}\mathbf{BS} + (\mathbf{E}_N\boldsymbol{\mu}\mathbf{BS})^T \tag{B2}$$

must negative semidefinite in order for the energy to decay at least as fast as its continuous counterpart. Following the analysis of *Dorostkar* [2012], we rewrite $\mathbf{A}$ as

$$\mathbf{A} = \tilde{\mathbf{A}} + \tilde{\mathbf{A}}^T = \left(\frac{\alpha_1}{2}\mathbf{E}_N\boldsymbol{\mu} + \mathbf{E}_N\boldsymbol{\mu}\mathbf{BS}\right) + \left(\frac{\alpha_1}{2}\mathbf{E}_N\boldsymbol{\mu} + \mathbf{E}_N\boldsymbol{\mu}\mathbf{BS}\right)^T \tag{B3}$$

and consider the conditions under which $\tilde{\mathbf{A}}$ is negative semidefinite (which depends on the operator $\mathbf{S}$). For our case (second-order accuracy on the boundary),

$$\tilde{\mathbf{A}} = -\frac{1}{h}\mathbf{E}_N\boldsymbol{\mu}\mathbf{T}_h \tag{B4}$$

where

$$\mathbf{T}_h = \begin{bmatrix} -\frac{\alpha_1 h}{2} - \frac{3}{2} & 2 & -\frac{1}{2} & & & & \\ 2 & -\frac{\alpha_1 h}{2} - \frac{3}{2} & 2 & -\frac{1}{2} & & & \\ -\frac{1}{2} & 2 & -\frac{\alpha_1 h}{2} - \frac{3}{2} & 2 & -\frac{1}{2} & & \\ & & & \ddots & & & \\ & & & -\frac{1}{2} & 2 & -\frac{\alpha_1 h}{2} - \frac{3}{2} & 2 & -\frac{1}{2} \\ & & & & -\frac{1}{2} & 2 & -\frac{\alpha_1 h}{2} - \frac{3}{2} & 2 \\ & & & & & -\frac{1}{2} & 2 & -\frac{\alpha_1 h}{2} - \frac{3}{2} \end{bmatrix}.$$

Stability follows if $\mathbf{T}_h$ is positive semidefinite. Applying the Gershgorin circle theorem, $\mathbf{T}_h$ is symmetric, positive semidefinite for $\alpha_1 \leq -\frac{13}{h}$ which completes the 1-D analysis for stability of the semidiscretization (8). Note that this technique for deriving constraints on α_1 is extendible to higher-order accurate SBP operators; however, one may find tighter bounds through the methods described in *Mattsson et al.* [2009]. It is also worthy to note that stability of these methods is gained by a particular type of transition to one-sided differences at the boundaries which can, in theory, reduce the order of accuracy of the method. We have used a second-order method at the interior and at the boundary, thus yielding a globally second-order accurate method. If one uses higher-order accurate methods, however, one generally obtains a method that is in fact higher than the lowest order obtained at the boundary (see *Svärd and Nordström* [2007, and references therein]).

For the 2-D analysis we also assume homogeneous boundary data $\mathbf{g}_f = \mathbf{g}_r = \mathbf{g}_s = \mathbf{g}_d = 0$, as done in section 2 (also see Appendix A). Taking $\alpha_s = -1, \alpha_d = -1$, and $\beta = 1$ simplifies (53) to

$$\frac{\mathrm{d}}{\mathrm{d}t}\left(\frac{1}{2}\mathbf{u}_t^T(\mathbf{H}_y \otimes \mathbf{H}_z)\boldsymbol{\rho}\mathbf{u}_t + \frac{1}{2}\mathbf{u}^T(\mathbf{M}_y^{\mu} + \mathbf{M}_z^{\mu})\mathbf{u}\right) = \tag{B5}$$

$$\mathbf{u}_t^T\left(\tilde{\mathbf{E}}_0\boldsymbol{\mu}\left[\left(\frac{\alpha_f}{2}\mathbf{I}_y + \mathbf{B}_y\mathbf{S}_y\right)\otimes\mathbf{H}_z\right] + \left(\tilde{\mathbf{E}}_0\boldsymbol{\mu}\left[\left(\frac{\alpha_f}{2}\mathbf{I}_y + \mathbf{B}_y\mathbf{S}_y\right)\otimes\mathbf{H}_z\right]\right)^T\right)\mathbf{u} \tag{B6}$$

$$+\mathbf{u}_t^T\left(\tilde{\mathbf{E}}_N\boldsymbol{\mu}\left[\left(\frac{\alpha_r}{2}\mathbf{I}_y + \mathbf{B}_y\mathbf{S}_y\right)\otimes\mathbf{H}_z\right] + \left(\tilde{\mathbf{E}}_N\boldsymbol{\mu}\left[\left(\frac{\alpha_r}{2}\mathbf{I}_y + \mathbf{B}_y\mathbf{S}_y\right)\otimes\mathbf{H}_z\right]\right)^T\right)\mathbf{u} \tag{B7}$$

where $\mathbf{E}_0 = \mathbf{e}_0^y\mathbf{e}^{y\,T}_0$, $\tilde{\mathbf{E}}_0 = \mathbf{E}_0 \otimes \mathbf{I}_z$, and $\mathbf{E}_N = \mathbf{e}_N^y\mathbf{e}^{y\,T}_N$, $\tilde{\mathbf{E}}_N = \mathbf{E}_N \otimes \mathbf{I}_z$.

Now consider the matrix

$$\tilde{\mathbf{B}} = \tilde{\mathbf{E}}_0\boldsymbol{\mu}\left[\left(\frac{\alpha_*}{2}\mathbf{I}_y + \mathbf{B}_y\mathbf{S}_y\right)\otimes\mathbf{H}_z\right] \tag{B8}$$

$$= -\frac{1}{h_y}[\tilde{\mathbf{E}}_0\boldsymbol{\mu}(\mathbf{T}_h \otimes \mathbf{H}_z)] \tag{B9}$$

where $\alpha_* = \alpha_f = \alpha_r$ and $\mathbf{T}_h$ is the symmetric matrix defined in the 1-D analysis above for $h = h_y$. As in section 3, our discretization is strictly stable if the semidiscrete problem dissipates energy at least as fast as its continuous counterpart. From the 1-D analysis, we know the conditions for which $\mathbf{T}_h$ is positive semidefinite. Since the matrix $\mathbf{H}_z$ is symmetric positive definite, $\tilde{\mathbf{B}}$ will be negative semidefinite under the same condition derived in the 1-D analysis, namely, $\alpha_* \leq -\frac{13}{h_y}$, and we have our energy estimate as described in section 3.

Appendix C: Truncating the Computational Domain

The computational domain must be artificially truncated in the $+y$ and $+z$ directions. We confirm here that our choice of domain size ($L_y = L_z = 24$ km) does not influence our results. We do this by doubling the size of the computational domain to $L_y = L_z = 48$ km, keeping all other parameters unchanged from those in Figure 9b, other than that we take $D_c = 16$ mm. We considered a larger value of D_c for computational ease as it furnishes a larger h^* which can thus be resolved with a coarser grid. Figure C1 compares these two simulations, zoomed in to the upper 24 km of the fault.

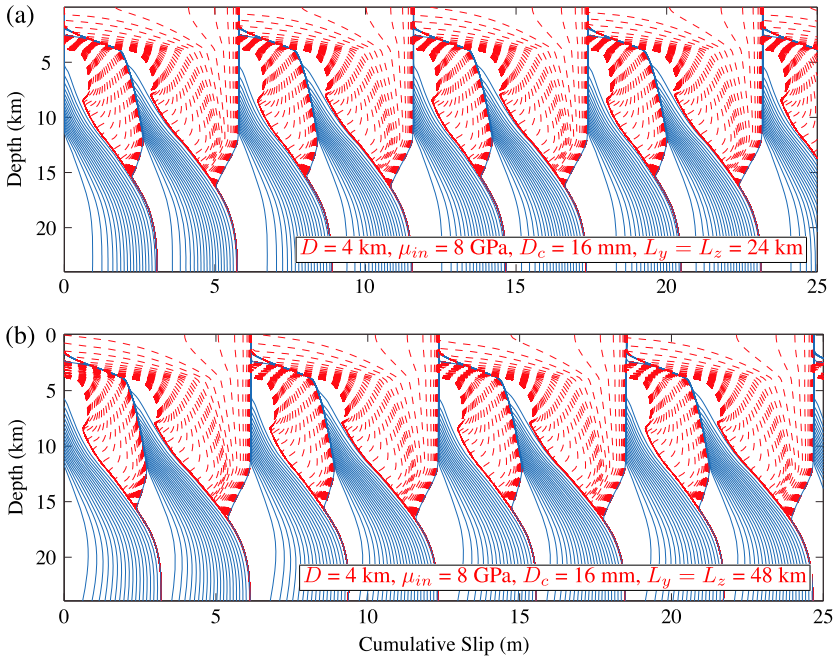

Figure C1. Snapshots of cumulative slip profiles for a 4 km deep basin ($D = H/3$) with D_c = 16 mm, μ_{in} = 8 GPa, and the size of computational domain doubled. $L_y = L_z$ = 48 km. Solid blue profiles plotted at 5-a intervals during interseismic period when max(V) ≤ 1 mm/s, dashed red profiles plotted at 1 s intervals during quasi-dynamic rupture.

Acknowledgments
This material is based upon work supported by the National Science Foundation under award 0948304 and by the Southern California Earthquake Center. SCEC is funded by NSF cooperative agreement EAR-0529922 and USGS cooperative agreement 07HQAG0008 (SCEC contribution 1796). The authors would like to acknowledge Jeremy Kozdon at the Naval Postgraduate School and Andrew Bradley and Leif Karlstrom at Stanford University for invaluable discussion. We also gratefully acknowledge the two anonymous reviewers and Associate Editor Jean-Paul Ampuero whose comments and suggestions much improved this work.

References

Ampuero, J.-P., and A. M. Rubin (2008), Earthquake nucleation on rate and state faults: Aging and slip laws, *J. Geophy. Res.*, *113*, B01302, doi:10.1029/2007JB005082.
Archuleta, R. J. (1984), A faulting model for the 1979 imperial valley earthquake, *J. Geophy. Res.*, *89*, 4559–4586.
Bilham, R. (1989), Surface slip subsequent to the 24 November 1987 Superstition Hills, California, earthquake monitored by digital creepmeter, *Bull. Seismol. Soc. Am.*, *79*, 424–450.
Dieterich, J. H. (1979a), Modeling of rock friction: 1. Experimental results and constitutive equations, *J. Geophy. Res.*, *84*, 2161–2168.
Dieterich, J. H., and K. B. Richards-Dinger (2010), Earthquake recurrence in simulated fault systems, *Pure Appl. Geophys.*, *167*, 1087–1104.
Dorostkar, A. (2012), Application of the perfectly matched layers in a discontinuous fluid media, Masters Thesis, Uppsala Univ. Sweden.
Engelder, J. T., J. M. Logan, and J. Handin (1975), The sliding characteristics of sandstone on quartz fault-gouge, *Pure Appl. Geophys.*, *113*, 69–86, doi:10.1007/BF01592900.
Erickson, B. A., and E. M. Dunham (2012), The effects of off-fault plasticity in earthquake cycle simulations, ABstract T34D-06 presented at 2012 Fall Meeting, AGU, San Francisco, Calif., 3–7 Dec.
Eriksson, S., and J. Nordström (2009), Analysis of the order of accuracy for node-centered finite volume schemes, *Appl. Numer. Math.*, *59*, 2659–2676.
Fay, N. P., and E. D. Humphreys (2005), Fault slip rates, effects of elastic heterogeneity on geodetic data, and the strength of the lower crust in the Salton Trough region, southern California, *J. Geophy. Res.*, *110*, B09401, doi:10.1029/2004JB003548.
Fialko, Y. (2006), Interseismic strain accumulation and the earthquake potential on the southern San Andreas fault system, *Nature*, *441*, 968–971, doi:10.1038/nature04797.
Fialko, Y., D. Sandwell, M. Simons, and P. Rosen (2005), Three-dimensional deformation caused by the Bam, Iran, earthquake and the origin of shallow slip deficit, *Nature*, *435*, 295–299.
Gu, J.-C., J. R. Rice, A. L. Ruina, and S. T. Tse (1984), Slip motion and instability of a single degree of freedom elastic system with rate and state dependent friction, *J. Mech. Phys. Solids*, *32*, 167–196.
Gustafsson, B., H.-O. Kreiss, and J. Oliger (1995), *Time Dependent Problems and Difference Methods*, 1st ed., Wiley, New York.
Hartzell, S., and T. Heaton (1983), Inversion of strong ground motion and teleseismic waveform data for the fault rupture history of the 1979 Imperial Valley, California, earthquake, *Bull. Seismol. Soc. Am.*, *73*(6), 1153–1184.
Hicken, J. E., and D. W. Zingg (2011), Superconvergent functional estimates from summation-by-parts finite-difference discretizations, *J. Sci. Comput.*, *33*, 893–922.
Kaneko, Y., and Y. Fialko (2011), Shallow slip deficit due to large strike-slip earthquakes in dynamic rupture simulations with elasto-plastic off-fault response, *Geophys. J. Int.*, *186*, 1389–1403.
Kaneko, Y., J.-P. Ampuero, and N. Lapusta (2011), Spectral-element simulations of long-term fault slip: Effect of low-rigidity layers on earthquake-cycle dynamics, *J. Geophys. Res.*, *116*, B10313, doi:10.1029/2011JB008395.
Kohli, A. H., and M. D. Zoback (2013), Frictional properties of shale reservoir rocks, *J. Geophy. Res.*, *118*, 5109–5125, doi:10.1002/jgrb.50346.
Kozdon, J. E., E. M. Dunham, and J. Nordström (2011), Interaction of waves with frictional interfaces using summation-by-parts difference operators: Weak enforcement of nonlinear boundary conditions, *J. Sci. Comput.*, *50*, 341–367.
Lapusta, L., and J. Rice (2003), Nucleation and early seismic propagation of small and large events in a crustal earthquake model, *J. Geophys. Res.*, *108*(B4), 2205, doi:10.1029/2001JB000793.
Lapusta, L., J. Rice, Y. Ben-Zion, and G. Zheng (2000), Elastodynamic analysis for slow tectonic loading with spontaneous rupture episodes on faults with rate-and-state dependent friction, *J. Geophys. Res.*, *105*(B10), 23,765–23,789.

Lindsey, E. O., and Y. Fialko (2013), Geodetic slip rate in the southern San Andreas Fault system: Effects of elastic heterogeneity and fault geometry, *J. Geophys. Res. Solid Earth*, *118*, 689–697, doi:10.1029/2012JB009358.
Lyons, S. N., Y. Bock, and D. T. Sandwell (2002), Creep along the imperial fault, Southern California, from GPS measurements, *J. Geophys. Res.*, *107*(B10), 2249, doi:10.1029/2001JB000763.
Mai, M. (2014), *Finite-source rupture model database*. [Available at http://equake-rc.info/SRCMOD/searchmodels/viewmodel/s1979IMPERI01ARCH/.]
Marone, C. (1998), Laboratory-derived friction laws and their application to seismic faulting, *Annu. Rev. Earth Planet. Sci.*, *26*, 696.
Marone, C., and C. H. Scholz (1988), The depth of seismic faulting and the upper transition from stable to unstable slip regimes, *Geophys. Res. Lett.*, *15*, 621–624, doi:10.1029/GL015i006p00621.
Mattsson, K. (2011), Summation by parts operators for finite difference approximations of second-derivatives with variable coefficients, *J. Sci. Comput.*, *51*, 650–682.
Mattsson, K., and J. Nordström (2004), Summation by parts operators for finite difference approximations of second derivatives, *J. Comput. Phys.*, *199*, 503–540.
Mattsson, K., F. Ham, and G. Iaccarino (2008), Stable and accurate wave-propagation in discontinuous media, *J. Comput. Phys.*, *227*, 8753–8767.
Mattsson, K., F. Ham, and G. Iaccarino (2009), Stable boundary treatment for the wave equation on second-order form, *J. Sci. Comput.*, *41*, 366–383.
Noda, H., and N. Lapusta (2013), Stable creeping fault segments can become destructive as a result of dynamic weakening, *Nature*, *493*, 518–521, doi:10.1038/nature11703.
Nordström, J. (2006), Conservative finite difference formulations, variable coefficients, energy estimates and artificial dissipation, *J. Sci. Comput.*, *29*(3), 375–404.
Nordström, J., K. Mattsson, and C. Swanson (2007), Boundary conditions for a divergence free velocity-pressure formulation of the navier-stokes equations, *J. Comp. Phys.*, *225*, 874–890.
Okubo, P. (1989), Dynamic rupture modeling with laboratory-derived constitutive relations, *J. Geophys. Res.*, *94*, 12,321–12,335.
Pollitz, F. F. (2012), Viscosim earthquake simulator, *Seismol. Res. Lett.*, *83*(6), 979–982.
Ranjith, K., and J. R. Rice (1998), Stability of quasi-static slip in a single degree of freedom elastic system with rate and state dependent friction, *J. Mech. Phys. Solids*, *47*, 1207–1218.
Rice, J. R. (1993), Spatio-temporal complexity of slip on a fault, *J. Geophy. Res.*, *98*, 9985–9907.
Rice, J. R., and A. L. Ruina (1983), Stability of steady-frictional slipping, *J. Appl. Mech.*, *50*, 343–349.
Rice, J. R., N. Lapusta, and K. Ranjith (2001), Rate and state dependent friction and the stability of sliding between elastically deformable solids, *J. Mech. Phys. Solids*, *49*, 1865–1898.
Roache, P. (1998), *Verification and Validation in Computational Science and Engineering*, 1st ed., Hermosa Publishers, Albuquerque.
Rockwell, T. K., and Y. Klinger (2013), Surface rupture and slip distribution of the 1940 Imperial Valley earthquake, Imperial Fault, Southern California: Implications for rupture segmentation and dynamics, *Bull. Seismol. Soc. Am.*, *103*(2A), 629–640, doi:10.1785/0120120192.
Ruina, A. (1983), Slip instability and state variable friction laws, *J. Geophys. Res.*, *88*, 10,359–10,370.
Rundle, J. B. (1988), A physical model for earthquakes: 2. Application to southern California, *J. Geophys. Res.*, *93*, 6255–6274.
Scholz, C. H. (1998), Earthquakes and friction laws, *Nature*, *391*, 37–42.
Scholz, C. H. (2002), *The Mechanics of Earthquakes and Faulting*, 2nd ed., Cambridge Univ. Press, Cambridge, U.K.
Sharp, R. V., et al. (1982), Surface faulting in the central Imperial Valley, *The Imperial Valley, California, earthquake of October 15, 1979, U.S. Geol. Surv. Prof. Pap. 1254*. pp. 119–143.
Shibazaki, B., and M. Matsu'ura (1996), Spontaneous processes for nucleation, dynamic propagation, and stop of earthquake rupture, *J. Geophy. Res.*, *101*, 13,911–13,917.
Sieh, K. (1996), The repetition of large-earthquake ruptures, *Proc. Natl. Acad. Sci.*, *93*(9), 3764–3771.
Strikwerda, J. C. (2004), *Finite Difference Schemes and Partial Differential Equations*, Society for Industrial and Applied Mathematics, Philadelphia, Pa.
Svärd, M., and J. Nordström (2007), On the order of accuracy for difference approximations of initial-boundary value problems, *J. Comput. Phys.*, *218*(1), 333–352.
Talebian, M., et al. (2004), The 2003 Bam (Iran) earthquake: Rupture of a blind strike-slip fault, *Geophys. Res. Lett.*, *31*, L11611, doi:10.1029/2004GL020058.
Tape, C., Q. Liu, A. Maggi, and J. Tromp (2009), Adjoint tomography of the southern California crust, *Science*, *325*, 988–992.
Tse, S. T., and J. R. Rice (1986), Crustal earthquake instability in relation to the depth variation of frictional slip properties, *J. Geophy. Res.*, *91*, 9452–9472.
Tullis, T. E., et al. (2012), Generic earthquake simulator, *Seismol. Res. Lett.*, *83*(6), 959–963.
Verberne, B. A., C. He, and C. J. Spiers (2010), Frictional properties of sedimentary rocks and natural fault gouge from the Longmen Shan fault zone, Sichuan, China, *Bull. Seismol. Soc. Am.*, *100*(5B), 2767–2790, doi:10.1785/0120090287.
Ward, S. N. (1996), A synthetic seismicity model for southern California: Cycles, probabilities, and hazard, *J. Geophy. Res.*, *101*, 22,393–22,418.
Weeks, J. D., and T. E. Tullis (1985), Frictional sliding of dolomite: A variation in constitutive behavior, *J. Geophy. Res.*, *90*(B9), 7821–7826, doi:10.1029/JB090iB09p07821.
Wei, M., Y. Kaneko, Y. Liu, and J. McGuire (2013), Episodic fault creep events in California controlled by shallow frictional heterogeneity, *Nat. Geosci.*, *6*(7), 566–570.
Zikanov, O. (2011), *Essential Computational Fluid Dynamics*, 1st ed., John Wiley, New York.